Overcrowding Drives Tumor Invasion by Inducing Nanotopographical Transition of Plasma Membrane

Xinbin Zhao[1, 9], Min Tan[2, 9], Long Li[3, 9], Xubo Lin[1], Zekun Li[4], Xiaohuan Wang[5], Bingqi Song[2], Zheng Guo[2], Tailin Chen[6], Sen Hou[2], Jiehou Fan[7], Shijiang Wang[8], Yun Zhang[4,*], Yubo Fan[1,2,*] and Jing Du[2,*]

1. Beijing Advanced Innovation Center for Biomedical Engineering, School of Engineering Medicine, Beihang University, Beijing 100191, China

2. Beijing Advanced Innovation Center for Biomedical Engineering, School of Biological Science and Medical Engineering, Beihang University, Beijing 100191, China

3. State Key Laboratory of Nonlinear Mechanics and Beijing Key Laboratory of Engineered Construction and Mechanobiology, Institute of Mechanics, Chinese Academy of Sciences, Beijing 100190, China; Center of Materials Science and Optoelectronics Engineering, University of Chinese Academy of Sciences, Beijing 100049, China

4. State Key Laboratory of Molecular Oncology, National Cancer Center/National Clinical Research Center for Cancer/Cancer Hospital, Chinese Academy of Medical Sciences and Peking Union Medical College, Beijing 100021, China

5. Department of Rehabilitation Medicine, Peking University Third Hospital, 49 North Garden Road, Beijing 100191, China.

6. School of Basic Medicine, Guangxi University of Chinese Medicine, Nanning 530200, China

7. Department of Breast Surgery, Second People's Hospital of Dezhou, Beijing 253000, China

`

8. Department of Radiation Oncology, Shandong Cancer Hospital and Institute, Shandong First Medical University, Shandong Academy of Medical Sciences, Jiyan Road 440, Jinan 250117, China

9. These authors contributed equally

*Correspondence: zhangyunbio@163.com (Y.Z.), yubofan@buaa.edu.cn (YB.F.), dujing@buaa.edu.cn (J.D.)

`

ABSTRACT

During the development from epithelial neoplasms to invasive carcinoma, uncontrolled growth and proliferation in a confined space cause tumor cells survive in a prolonged overcrowding condition. However, the role of this aberrant physical stimulus induced by overcrowding in the invasiveness acquisition of epithelial cells remains unclear. Here, we first identified overcrowded cancer cells were more abundant at invasive foci in human cancer samples and mouse xenograft models. Combining with mechanical modelling, genetic manipulations and biophysical measurements, we revealed that prolonged overcrowding induces retentive invasiveness in cancer cells by triggering nanocorrugated topographic transition of plasma membrane. Further study demonstrated that the nanocorrugated topographic transition is induced by overcrowding-increased Laplace pressure and disrupts lipid raft-like domains organization to promote tumor invasion. Finally, suppressing nanocorrugated topographical transition of plasma membrane by strengthening membrane-cortex-attachment resists to tumor cell invasion in a mouse model of oncogenesis. This work reveals the profound effect of tissue-scale mechanical revolution-induced biophysical transition of cancer cells in driving tumor invasion.

`

INTRODUCTION

Mechanical force modulates embryonic development, influences tissue homeostasis, and contributes to disease like cancer[1-3]. The primary tumor microenvironment (TME) is characterized by a diverse array of harsh mechanical cues, including increased matrix stiffness and solid and fluid stresses. However, unlike the extensive research on the effects of matrix stiffness on tumor pathology, the involvement of solid stress in tumor initiation and progression is less understood.

Uncontrolled growth and proliferation of tumor cells pushes and displaces the surrounding normal tissue, which in turn constrains tumor expansion leads to overcrowded tissues and generates mechanical compressive stress within solid tumor and surrounding extracellular matrix (ECM)[4-6]. Recent studies in mouse models of skin tumor reveal that constraining forces from overlying suprabasal tumor cells and underlying ECM shape tissue architecture and affect tumor initiation and progression[4,7]. Strong confinement has been shown to drive a fast amoeboid migration in mesenchymal cells and embryonic progenitor cells[8,9]. Cell nucleus is able to sense constraining forces and responds to it by switching to a rapid migratory mode that enables tumor cells to squeeze out from compression conditions[10,11]. Strong confinement also causes nuclear deformation, which results in localized nuclear envelope rupture and DNA damage in tumor cells, which facilitates the invasive phenotype of tumor cells[12]. Collectively, these studies shed light into the profound influence of cell nucleus in tumor cell behaviors by constraining forces. However, the understanding of how the plasma membrane mechanically respond by deforming from

`

constraining forces, is an important first step to further investigate how these mechanical stimuli are eventually transmitted to the cell nucleus. Moreover, the mechanical adaptability of cancer cells to the prolonged compressive stress under overcrowded condition and its function in the acquisition of invasive phenotype remain unclear.

Further, recent studies have reported the ability of cells to remember the mechanical stimuli after the cessation of force, which is termed “mechanomemory”[13]. Cancer cells not only adapt to mechanical cues, such as stiffness, in the primary TME and also retain the biophysical adaptations induced by these physical stresses after they move to a new environment[14,15]. However, whether the substantial long priming time of compressive stress in the overcrowded primary tumor tissue could imprint mechanical memory in cancer cells has not been studied.

In this study, we first identified a nanosmooth-to-nanocorrugated transition of cell plasma membrane in invasive foci wherein cells experience overcrowding stimuli in human cancer samples and mouse xenograft models. Using a spontaneously overcrowding gradient model of growing epithelial cancer cell sheets, we found that prolonged overcrowding induces retentive invasiveness in cancer cells. Combining with mechanical modelling, genetic manipulations and biophysical measurements, we found that overcrowding-increased Laplace pressure triggers membrane topographic transition from nanosmooth to nanocorrugated state which disrupts lipid raft aggregation and drives tumor invasion. Finally, we demonstrated that suppressing nanocorrugated topographical transition of plasma membrane by enhancing

`

membrane-cortex-attachment resists to cancer cell invasion in a mouse model of oncogenesis.

`

RESULTS

Overcrowding induces retentive invasiveness in cancer cells

We first observed human samples of hyperplastic skin, cervix and breast tissues *in situ* with immunofluorescence staining of RAB5A as a micro-invasive marker[8]. Compared with cells located in the tumor bulk, cells located in the invasive foci exhibited significant higher cell density, indicating an overcrowding microenvironment (Fig. 1a,b, S1a-f). To examine the link between cellular overcrowding and tumor invasion, we developed a xenograft mouse model by subcutaneous injection of HeLa cells expressing EYFP-mem into nude mice (Fig. 1c). By 10 days, small masses had formed at the back skin. Immunofluorescence staining of RAB5A demonstrated the stroma adjacent to the invasive edge displayed a higher cell density than the stroma associated with the rest of the cancer cells, especially for in situ advanced tumor (Fig. 1d-f). These results suggest that tumor cells at the periphery of the stroma exhibit pronounced crowding associated with tumor invasion.

To unveil the function of overcrowding conditions in the progression of tumor invasion, we developed a spontaneous overcrowding model composed of a freely growing monoclonal cell sheet (Fig. 1g). We have previously shown that during cell proliferation, the cell sheet spontaneously displayed a progressive overcrowding gradient radiating from the central region to the peripheral region resulted from the interfacial shear stress between cell sheet and substrate[16]. The extent of overcrowding was indicated by crowding strain (calculated by $(A_0-A_n)/A_0$, A_0 is the nuclear area of cells in sparse culture, and A_n is the nuclear area of cells in the cell sheet, Fig. 1h).

`

According to the values of crowding strain, the cell sheet was segmented into high crowding or overcrowding (HC: crowding strain from 0 to 0.3) and low crowding (LC: crowding strain from -0.3 to 0) regions (Fig. 1i). The transwell invasion assay showed that cells located in the HC region displayed significantly elevated invasiveness compared with cells located in the LC region in various cancer cell lines, including HeLa, MC38 and A431 (Fig. 1j and k). Time-lapse imaging of NLS-GFP^{+} HeLa cell sheets showed that cell invasion was first observed in the HC region (Fig. S2a and b), indicating the preferential initiation of invasion in overcrowded cells.

As the invasion processes require degradation of basement membrane[17], we then tested whether overcrowding affects ECM degradation using Cy5-conjugated gelatin hydrogels coated on culture dishes. The vertical cross-sectional (XZ-plane) images showed that the thickness of ECM was gradually reduced with increased crowding strain (Fig. S2c and d), indicating that overcrowding promotes degradation of ECM by cancer cells. Moreover, immunofluorescence staining of cortactin (an actin-bundling protein enriched in invadopodia[18,19]) showed that the number of invadopodia *per* cell was gradually elevated with the increase of crowding strain in cells grown on matrigel-coated culture dishes (Fig. S2e and f). These results suggest that prolonged overcrowding induced by cell proliferation promotes cancer cell invasion.

Recent studies have reported the ability of cells to remember the mechanical stimuli after the cessation of force, which is termed “mechanomemory”[20,21]. So, we proceed to investigate whether the overcrowding-induced invasiveness will be retained after

`

cells leaving the overcrowded microenvironment. Cells were grown (primed) for different times (priming time) in high-crowding or low-crowding culture, and subsequently collected and transferred to a sparse culture (crowding strain is around 0) for indicated times (memory time) (Fig. 1l). The transwell invasion assay showed that cells primed in high-crowding culture for 3 or 5 days exhibited significantly elevated invasiveness after 1 day of sparse culture compared with low-crowding-primed cells (Fig. 1m and n), indicating a duration-dependent mechanical memory imprinting.

Next, to test the memory longevity of overcrowding, cells were primed for 5 days in high-crowding or low-crowding culture, followed by exposure to sparse culture for different times (1, 2, 3, or 7 days). The transwell invasion assay showed that cells primed in high-crowding culture retained stronger invasiveness even after 2 days of sparse culture compared with low-crowding-primed cells (Fig. 1o and p). We then compared the memory longevity of overcrowding for different priming time up to 20 days. As shown in Fig. 1q, the retention time of enhanced invasiveness in a high-crowding-primed cells was increased with priming time. Specifically, cells primed in high-crowding culture for 20 days retained facilitated invasiveness even after 7 days of sparse culture. These results suggest that prolonged exposure to overcrowding causes extended retention of invasiveness.

Further experiments demonstrated that high-crowding-primed cells for 5 days exhibited significantly elevated number of invadopodia *per* cell than low-crowding-primed cells even after 1, 2, or 3 days of sparse culture (Fig. 1r and s). Similar retention of mechanical memory longevity was observed in the ECM

`

degradation ability of high-crowding-primed cells (Fig. 1t and u). This retentive invasiveness of high-crowding-primed cells was consistently observed in other cell types, such as A431 cells, a human skin cancer cell line (Fig. S3a and b). Together, these results suggest that overcrowding drives retentive invasiveness in cancer cells.

To further identify the cell state after bearing overcrowding stimulus, cells growing in LC or HC regions were again collected respectively, followed by SMART-seq II to assess the transcriptional profiles. We identified 1991 genes that changed consistently in three HC groups compared with LC groups (Fig. S4a). Furthermore, comparison analysis to identify significantly altered genes revealed 1208 up-regulated proteins and 783 down-regulated genes in the 1991 genes (Fig. S4b). Notably, an increased trend of EMT-activating transcription factors[22], such as Snail, Zeb1, and TwistNB mRNA expression were observed in HC cells compared with LC cells (Fig. S4c). Moreover, cells experiencing high crowding displayed greater mRNA levels of ADAM9 and ADAM10, which belong to membrane-anchored metalloproteases and promotes ECM degradation (Fig. S4c). The expression levels of adhesions junction components N-cadherin (CDH2) were upregulated in high crowded cells compared with low crowded cells (Fig. S4c). However, there is no significant difference for E-cadherin (CDH1) expression, suggesting a partial EMT phenotype in high crowding cells. Immunofluorescence staining showed that the protein levels of Snail and Twist were gradually induced with increased crowding strain (Fig. S4d-g). These results indicate that overcrowding induces retentive invasiveness in tumor cells.

`

Overcrowding triggers retentive nanocorrugated topographical transition of plasma membrane by increasing Laplace pressure

Previous work suggested that the nucleus underwent an elastic deformation under mechanical stress and physical space constraints. In fact, cell plasma membrane firstly senses shape deformations in crowded environment. Therefore, we assessed the morphology of human skin cancer tissues, we found a strong deformation of plasma membrane in overcrowding-exposed cells at the invasive edge compared with those in low-crowding-exposed cells in the tumor bulk (Fig. 2a). Fractal analysis revealed that the plasma membrane of overcrowding-exposed cells showed significantly higher values of fractal dimension than plasma membrane of low-crowding-exposed cells (Fig. 2b). Similar deformation of plasma membrane in overcrowding-exposed cells located in invasive foci were observed in cervical and breast cancer tissues (Fig. S5a-d). Like human samples of hyperplastic breast, skin and cervix tissues in situ, plasma membrane deformation were mostly found at the periphery of the tumor mass, especially in those enriched in micro-invasive foci in mouse xenografts (Fig. 2c and d). These results indicate a severe deformation of cell plasma membrane in invasive foci wherein cells exposed to overcrowding microenvironment.

To investigate the effects of overcrowding on the topographic structures of cell membrane, we analyzed the plasma membrane morphology of HeLa cells expressing EYFP-mem experiencing different crowding strains. The apical membrane of cells exposed to high crowding strain showed much higher curvature than those exposed to low crowding strain (Fig. 2e, f). 3D confocal imaging showed that

`

overcrowding-exposed cells exhibited enhanced protrusions at the apical side of plasma membrane in contrast to the much smoother topography of apical membrane in control (low-crowding-exposed) cells (Fig. 2g, h), indicating a nanocorrugated topographic transition of plasma membrane triggered by overcrowding.

Using scanning electron microscopy (SEM) and transmission electron microscope (TEM) imaging, we revealed an enrichment of nanoscale protrusions at the apical plasma membrane in overcrowding-exposed cells compared to low-crowding-exposed cells (Fig. 2i, j). The nano-topological morphology of plasma membrane was further measured by atomic force microscopy (AFM). The average roughness (Ra) and root mean square roughness (Rq) as well as cellular height are all significantly increased in cells exposed to overcrowding compared to cells experiencing low crowding strain (Fig. 2k-n). Notably, consistent with the retentive invasiveness in cells priming by overcrowding, cells primed in high-crowding culture for 5 days retained elevated cell protrusions (filopodia) even after 7 days of sparse culture compared with low-crowding-primed cells (Fig. 2o-q). Together, these results demonstrate that prolonged overcrowding triggers retentive nanocorrugated topographic transition of plasma membrane in cancer cells.

To figure out the mechanism underlying nanotopographical transition of cell plasma membrane triggered by overcrowding, we first measured the tension of plasma membrane which has been reported to control plasma membrane morphology[23]. By analyzing the lifetime of a live cell fluorescent membrane tension probe Flipper-TR[24], we found that the tension of apical membrane in cells exposed to overcrowding was

`

significantly decreased compared with that in low-crowding-exposed cells (Fig. 3a, b), indicating that the tension of plasma membrane is reduced by overcrowding.

It has been demonstrated that plasma membrane tension is dependent on the contractility of the underneath actin cortex[25]. By fluorescence resonance energy transfer (FRET)-based biosensors[26,27], we analyzed the activity of Rho GTPases which are master regulators of actomyosin structure and dynamics. The activity of RhoA at the apical side was significantly decreased in high-crowding-exposed cells compared with low-crowding-exposed cells. By contrast, the activity of Rac1 was increased in high-crowding-exposed cells (Fig. 3c, d). Since RhoA contributes to the assembly of stress fibers[28], while Rac1 is a highly characterized GTPase that mediates branched actin polymerization[29], these results indicate that overcrowding may affect filamentous actin (F-actin) cytoskeletal remodeling.

To assess whether the organization of actin network underlying the apical plasma membrane (actin cortex) was regulated by overcrowding, we performed 3D confocal imaging of F-actin and found that the orientation of actin fibers was altered by overcrowding which is e by an angle more vertical (> 70°) related to the base plane in cells exposed to overcrowding whereas an angle mainly parallel (< 20°) in cells experiencing low-crowding strain (Fig. 3e and f). Similar results were found in A431 cells (Fig. S6a and b). Moreover, the height of apical F-actin was significantly increased in high-crowding-exposed cells compared with low-crowding-exposed cells (Fig. 3g). These results suggest that overcrowding triggers remodeling of the apical actin cortex.

`

Previous studies have established the regulation of membrane-to-cortex attachment (MCA) and cell protrusions (such as blebs) by the Laplace pressure which is the pressure difference across the plasma membrane[30]. As an essential regulator of cell shape and mechanics, the Laplace pressure affects various cellular processes, including cell migration, proliferation, necrosis, and apoptosis, as well as material transportation and signal transduction[30]. To investigate the biophysical mechanism underlying membrane nano-topological transition induced by overcrowding, we analyzed the Laplace pressure in cells exposed to different crowding strains using a micro pressure system[31]. The Laplace pressure in cells exposed to high-crowding strains was observed to be significantly higher than that of cells subjected to low-crowding strains (Fig. 3h and i). Since the hydrostatic pressure outside the cell remains consistent between high-crowding-exposed cells and low-crowding-exposed cells, these s indicate that overcrowding causes an increase in the Laplace pressure.

To explore the morphology of plasma membrane in response to the Laplace pressure and and the lateral tension, we performed systematic Monte Carlo (MC) simulations (Fig. 3j). The resulting snapshots from Fig. 3k clearly showed that higher Laplace pressure $\Delta\overline{p}$ or lower lateral tension $\overline{\tau}$ contributes to more pronounced bulges and larger deformations. Quantitatively, we measured the relative roughness $\overline{\xi}_{\perp}$ of the cell membrane as a function of both Laplace pressure and lateral tension. The relative roughness $\overline{\xi}_{\perp}$ became larger with higher $\Delta\overline{p}$ and lower $\overline{\tau}$ (Fig. 3l). These results suggest that the nanoscale topography of plasma membrane is regulated by Laplace pressure and lateral tension.

`

Notably, we found that the proportion ϕ of linker proteins that bound membrane to the cortex decreases accompanied by higher $\Delta\overline{p}$ and lower $\overline{\tau}$ (Fig. 3m). Increasing the number of linker proteins substantially reduced the membrane roughness under constant $\Delta\overline{p}$ and $\overline{\tau}$ (Fig. 3n), indicating the essential role of membrane-to-cortex attachment in the regulation of membrane topography by Laplace pressure and lateral tension. In summary, these results suggest that the nanocorrugated topographical transition of plasma membrane might result from the membrane-to-cortex detachment due to the increase in Laplace pressure and decrease in membrane tension in overcrowding-exposed cells.

Suppressing nanocorrugated topographical transition of plasma membrane by enhancing membrane-to-cortex attachment abrogates overcrowding-induced cancer cell invasion

To validate the results of simulations, we examined the distribution of linker proteins (ezrin, radixin, and moesin ((ERM)) family proteins) mediating the membrane-to-cortex attachment which has been demonstrated to constrain cancer cell dissemination[32] Immunofluorescence staining showed that the intensity of phosphorylated ERM (pERM, an active membrane- and actin-bound form of ERM proteins) signals at the apical membrane was gradually reduced along with increased crowding strain (Fig. 4a, b), suggesting that overcrowding inhibits the activity and distribution of ERM. In addition, pERM distribution at apical side of cells primed in high-crowding culture shown a gradual recovery after sparse culture compared with

`

low-crowding-primed cells (Fig. 4c, d).

Our above simulation results have suggested that enhanced ERM-mediated MCA resists to the nanocorrugated topographical transition triggered by overcrowding (Fig. 3n). To experimentally explore the function of MCA, we used a Lyn-FRB and $Ezrin_{abd}$-FKBP activation system[25] containing a constitutively active F-actin binding domain of Ezrin ($Ezrin_{abd}$T567D). Upon addition of rapamycin, $Ezrin_{abd}$T567D was recruited to the membrane and increased the density of membrane proximal F-actin (Fig. 4e, S7a-b). Acute reinforcing MCA by recruitment of FKBP-$Ezrin_{abd}$T567D to plasma membrane after rapamycin treatment markedly reduced protrusions at the apical side of plasma membrane and F-actin height indicated by 3D confocal imaging (Fig. 4f-g, S7c-d). These results suggest that overcrowding triggers plasma membrane nanocorrugated topographical transition by inhibiting ERM-mediated MCA.

Next, we pursued whether enhanced MCA resists to cancer cell invasion induced by overcrowding. The transwell invasion assay showed that enhanced MCA by FKBP-$Ezrin_{abd}$T567D activation significantly prohibited cell invasion in overcrowding-exposed cells (Fig. 4h and i). Immunofluorescence staining of cortactin at the basal membrane showed that the number of invadopodia *per* cell was significantly decreased by FKBP-$Ezrin_{abd}$T567D activation in high-crowding-exposed cells (Fig. 4j-l). Furthermore, FKBP-$Ezrin_{abd}$T567D activation also prohibited the degradation of ECM by cancer cells exposed to overcrowding (Fig. 4m-o). These results suggest that suppressing nanocorrugated topographical transition of plasma membrane by enhanced ERM-mediated MCA rescues the overcrowding-driven

`

invasion of cancer cells.

Overcrowding-triggered nanocorrugated topographical transition of plasma membrane promotes cancer cell invasion by disrupting lipid raft-like domains organization

So far, we have demonstrated the effects of overcrowding on plasma membrane nanotopology and its involvement in cancer cell invasion. Next, we proceeded to explore the mechanism underlying the regulation of cancer cell invasion by plasma membrane nanotopological transition. Accumulative evidence has indicated that the plasma membrane consists of many lipid microdomains enriched in cholesterol and sphingolipid. These liquid microdomains are often termed lipid rafts which undergo dynamic fission, fusion and redistribution processes, and are believed to be involved in many physiological and pathological activities by coalescing into a larger signaling platform[33-35]. To investigate the potential role of lipid raft-like domains in cancer cell invasion triggered by overcrowding, we first analyzed the distribution of lipid raft-like domains in response to Laplace pressure and lateral tension using MC simulations. Upon incorporating lipid raft-like domains into our computational model, we found that raft-like domains distribution changes with the Laplace pressure $\Delta\overline{p}$ and the lateral tension $\overline{\tau}$. For small $\Delta\overline{p}$, raft-like domains coalesce into one single mesoscopic domain. Increasing the Laplace pressure causes separation of a single mesoscopic domain into multiple small domains (Fig. 5a). Further, we calculated the pair distribution function g(r) to quantitatively describe the spatial distribution of lipid

`

raft-like domains in cell membrane. A larger value of g(r) means a higher probability of finding two raft patches with a distance r. As shown in Fig. 5b, as $\Delta\overline{p}$ increases, $g(\mathrm{r})$ decreases at smaller values of r. This result manifests that the tendency for raft coalescence is hindered by the increased Laplace pressure. A further comparison of the pair distribution function showed that increase in the lateral tension leads to an increase in $g(\mathrm{r})$ at smaller values of r, indicating that enhanced membrane tension contributes to the raft coalescence (Fig. 5b). These results demonstrate that the higher the Laplace pressure or the smaller the membrane tension, the less clustered the lipid raft-like domains.

To understand the regulatory mechanism of lipid raft-like domains distribution by pressure and tension, we estimated the bending energy of the multicomponent membrane. At small raft-raft contact energy U, the lipid rafts distribute more-or-less uniformly within the cell membrane. At large U, these lipid rafts tend to coalesce into one single mesoscopic domain. Fig. 5c shows that the change of bending energy ΔE_{b} increases with the raft-raft contact energy U, indicating the raft coalescence is energetically disfavorable. The higher the Laplace pressure or the smaller the lateral tension, the larger the energy change ΔE_{b}, *i.e.*, the more the energetic cost for raft coalescence. This bending energy consideration helps to explain our findings that the lateral tension facilitates the raft aggregation in cell membrane, whereas the opposite is true for the Laplace pressure.

Further, we investigated the lipid raft-like domains redistribution in response to the increased area concentrations of linker proteins. The size distribution of raft clusters

`

in Fig. 5d shows that the first peak moves leftward, while the second peak shifts rightward with increasing the area concentration of linker proteins. These findings indicate that the increase of area concentration of linker proteins contributes to the aggregation of lipid raft-like domains into larger clusters.

To experimentally verify the results from simulation, the abundance of lipid raft-like domains in cells exposed to different crowding strains was observed using Cy5-conjugated cholera toxin subunit B (CTxB) which specifically binds to lipid raft-enriched GM1 ganglioside[36]. The fluorescence imaging showed that CTxB-labeled lipid raft-like domains at the apical membrane was dramatically reduced in high-crowding-exposed cells compared with low-crowding-exposed cells (Fig. 5e and f). Specifically, both the fluorescent intensity of CTxB and the size or number *per* cell of CTxB clusters at the apical membrane displayed a crowding-strain-dependent reduction after crowding strain exceeds 0 (Fig. 5g-i). Furthermore, immunofluorescence staining with Flotillin-1, Caveolin-1, and Cavin-1 showed that both of the two types of lipid raft-like domains (*i.e.*, flotillin-rich planar lipid rafts and caveolin-rich caveolae[34]) exhibited a crowding-strain-dependent decrease at the apical membrane (Fig. 5j-o). Transcriptional profiles analyzed by SMART-seq II showed that the expression levels of key genes involved in flotillin-rich planar lipid rafts and caveolin-rich caveolae were significantly reduced in high-crowding-exposed cells compared with low-crowding-exposed cells (Fig. 5p and q). Quantitative RT-PCR also demonstrated a drastic downregulation of caveolin-1, cavin-1, and flotillin-1 mRNA expression in cells exposed to high crowding strain

`

(Fig. 5r). These results suggest that the organization of lipid raft-like domain organization of plasma membrane in cancer cells are interrupted by overcrowding.

Since lipid raft availability is regulated by alterations in lipid metabolism, we next assessed the levels of cholesterol and GM1 ganglioside in overcrowding-exposed cells. However, the fluorescent filipin III staining showed little significant change in free cholesterol levels between low-crowding-exposed cells and high-crowding-exposed cells (Fig. S8a, b). Immunofluorescence staining of GM1 ganglioside also showed that the level of GM1 ganglioside at the apical plasma membrane did not alter in cells subjected to different crowding strains (Fig. S8c, d). These results suggest that overcrowding does not influence the levels of main components within lipid rafts in cancer cells.

According to our simulation results, in overcrowding-exposed cells, increased Laplace pressure and reduced lateral tension induce nanocorrugated topographical transition of plasma membrane (Fig. 3k-n) and prohibits the aggregation of lipid raft-like domains in cell membrane (Fig. 5a-d). Thus, we further investigated the regulation lipid raft-like domains by plasma membrane nanotopology. We first found that CTxB labeled lipid raft-like domains at the apical membrane were gradually reduced along with increases in membrane curvature (Fig. 6a, b). Moreover, enhanced MCA by FKBP-Ezrin$_{abd}$T567D activation significantly increased the accumulation of lipid raft-like microdomains at the apical plasma membrane indicated by both fluorescent intensity and the number of CTxB clusters *per* cell in overcrowding-exposed cells (Fig. 6c-f). These results suggest that lipid raft-like

`

microdomains are disrupted by the nanocorrugated topographical transition of plasma membrane in overcrowding-exposed cells.

Recent study demonstrated that the lipid raft-like domains aggregation is strongly dependent on the local nanoscale topographic configuration of the plasma membrane by using synthetic membrane system[37]. To further explore the effect of membrane curvature on the aggregation of lipid raft-like domains, we performed μs-scale coarse-grained (CG) molecular dynamics (MD) simulations of two three-component vesicles (DPPC: 50%; DUPC: 30%; CHOL: 20%) with different radii (10 nm and 20 nm) using Martini CG model. As shown in the system snapshots and normalized lateral contacts of DUPC lipids (Fig. 6g, h), DPPC/DUPC/CHOL vesicles had the obvious liquid-liquid phase separation in both cases. Meanwhile, the larger vesicle (r = 20 nm), which has a lower membrane curvature, exhibited a substantially enhanced phase separation. In other words, the local nanocorrugated topography of the cell membrane will inhibit its liquid-liquid phase separation. The above results suggest that overcrowding disrupts the aggregation of lipid raft-like domains by causing nanocorrugated topography of plasma membrane.

To examine whether the disruption of lipid raft-like microdomains is involved in the enhanced invasiveness of overcrowding-exposed cancer cells, the lipid raft-like domains were modified by exogenous cholesterol addition or methyl-β-cyclodextrin (MβCD) treatment to enrich or deplete membrane cholesterol content, respectively. The transwell invasion assay showed that cholesterol addition significantly inhibited cell invasion. In contrast, cholesterol depletion by MβCD significantly enhanced the

`

invasiveness in both high-crowding-exposed cells and low-crowding-exposed cells (Fig. 6i, j). Exogenous cholesterol addition and MβCD treatment both reduced the difference in cell invasiveness between high-crowding-exposed cells and low-crowding-exposed cells (Fig. 6j). Moreover, exogenous cholesterol addition or MβCD treatment significantly decreased or increased the number of invadopodia *per* cell, respectively and blocked the difference between high-crowding-exposed cells and low-crowding-exposed cells (Fig. 6k, l). Taken together, these results suggest that overcrowding drives cancer cell invasion by nanocorrugated topographic of plasma membrane which disrupts lipid raft-like domain aggregation.

Extensive studies have demonstrated that the carcinomas and their invasion are correlated with the loss of epithelial organization and disruption of cell-cell contact has been demonstrated to promote cancer invasion[38]. Cholesterol-rich membrane domains at the apical junctions is required for tight junction formation[39]. In our experiments, we found that the accumulation of Claudin-1 (a tight junction component[40]) at the apicolateral membrane was gradually declined as crowding strain increased (Fig. 6m and n). Moreover, the fluorescent intensity of CTxB was positively correlated with Claudin-1 level (Fig. 6m and n). Specifically, CTxB-labeled lipid raft-like domains at the apical membrane mainly existed in cells with strong Claudin-1 intensity at the apicolateral membrane (Fig. 6m). These results suggest that disruption of epithelial integrity by lipid raft-like domain disorganization may contribute to cancer cell invasion driven by overcrowding-triggered membrane nanotopographic transition.

`

Suppressing nanocorrugated topographical transition of plasma membrane resists to tumor invasion in a xenograft mouse model

To further evaluate the role of nanocorrugated topographical transition in the invasive behavior of crowded tumor cells *in vivo,* we established a subcutaneous mouse xenograft model using FKBP-Ezrin$_{abd}$T567D HeLa cells (Fig. 7a). This xenograft can be used to examine the invasive growth pattern but not constitute a metastasis model. After 1 week of tumor growth, mice were treated with rapamycin via i.p. three times *per* week. Two-week administration of rapamycin completely recruited Ezrin$_{abd}$T567D to the cell membrane in tumor tissue (Fig. 7b and c). To measure the effect of enhancing membrane to cortex attachment on membrane topography of tumor cells *in vivo*, we analyzed fractal dimension of tumor cells in the xenograft mice after rapamycin treatment. Inhibiting membrane to cortex detachment by rapamycin significantly lowered fractal dimension of plasma membrane, suggesting that nanocorrugated topographical transition of plasma membrane could be effectively suppressed through enhancing membrane to cortex attachment *in vivo* (Fig. 7d and e).

Furthermore, we found lipid raft markers Caveolin-1 and Flotillin-1 level increased in FKBP-Ezrin$_{abd}$T567D HeLa cells of the xenograft mouse treated by rapamycin (Fig. 7f-i), suggesting that enhancing membrane to cortex attachment *in vivo* could improve lipid raft-like domains stability. Next we observed that tumors from mice without treatment of rapamycin exhibited primarily deeper invasion toward the muscle layer as supported by microscopic analysis of hematoxylin and eosin-stained

`

sections (Fig. 7j and k). In contrast, the majority of rapamycin-treated tumors presented a predominantly cohesive pushing front that clearly segregated tumor cells from the surrounding muscle layer with only minor focal invasions (Fig. 7k), demonstrating that rapamycin remarkably alters the invasion pattern. These results suggest that suppressing nanocorrugated topographical transition of plasma membrane by enhancing MCA resists to tumor cell invasion.

In summary, our experiments and modeling results demonstrate that overcrowding induces nanotopographical transition of plasma membrane through cell interior pressure-reduced membrane to cortex detachment. Nanocorrugated topographical transition promotes cancer cell invasion by disrupting lipid raft-like domains organization. In addition, reinforcing membrane to cortex attachment by ERM proteins resists to the overcrowding-induced invasion of tumor cells (Fig. 8).

`

DISCUSSION

As growing in confined spaces, cancer cells push and stretch solid components of the surrounding tissue and thus experience situations of overcrowding[6]. Recent studies have shown that overcrowding triggers cell extrusion to maintaining epithelial homeostasis or induces cell migration during embryonic development [1,41,42]. However, the effect of overcrowding on the progression of tumor invasion remains an open question. Here, using a spontaneously overcrowding gradient model of growing epithelial cancer cell sheet, we revealed that prolonged overcrowding drives cancer cell invasiveness acquisition through triggering membrane topographic transition from nanosmooth to nanocorrugated state. Combining with mechanical modelling, genetic manipulations and biophysical measurements, we further found that overcrowding-triggered membrane topographic transition disrupts lipid raft aggregation to drive tumor invasion. Moreover, the acquired invasiveness driven by overcrowding could be retained as "mechanomemory" in cancer cells (Fig. 8).

Plasma membrane and nuclei of cancer cells always exhibit complex and irregular shapes and fractal geometry is already used to efficiently estimate the geometrical shapes observed in tumor growth and the correlation to the pathological process[43]. For example, the skin cancer can be modeled by calculating fractals to detect the invasiveness of tumor cells[43]. The fractal dimension of AFM maps is analyzed for three stages of progression towards cervical cancer, from normal through immortal to malignant cells[44]. However, the mechanism underlying these topographical alterations in cancer cells and their function in cancer invasion remain unknown. Here, we

`

identify that progressive overcrowding induces nano-protrusions at the apical plasma membrane of cancer cells by increased Laplace pressure which disrupted epithelial integrity through suppressing lipid raft aggregation.

Although the controversies about the composition, properties, and even the existence of lipid rafts remain unresolved[45], the fact that most of transmembrane proteins were found in lipid rafts to serve as signaling platforms or connect actin cytoskeleton for controlling cell behaviors is widely studied[46]. A study found that invadopodia formation and extracellular matrix degradation required stable lipid rafts in human breast cancer cells[47]. However, considering crowded tumor microenvironment and high membrane dynamics, lipid raft will experience phase separation by assembly and disassembly. The topographic configuration is an important machinery for controlling the lipid raft phase separation in model membranes. Macroscopic lipid raft domain exist in a region with nanosmooth topography[37], which is in agreement with our observation. Pharmacological raft disruption using MβCD decreases CD44 retention inside lipid rafts and promotes CD44 relocalization outside lipid rafts and interaction with ezrin to drive cell migration[48]. In addition, oncogenic mutants of RAS proteins (encoded by *HRAS, KRAS, NRAS*) are localized to the inner leaflet of the PM and the assembly of RAS nanoclusters depend on the interactions between PM lipids and RAS molecules[49]. Active NRAS.GTP distribute to the domain boundary between liquid-ordered (L_o) and liquid-disordered (L_d) domains, but active HRAS.GTP, active KRAS4A and active KRAS4B all distribute to the L_d domains[50]. The RAS activation can be driven by

`

lipid-mediated nanoclustering because of disrupted lipid raft phase separation through fractal topology of plasma membrane.

Our experiments have demonstrated that plasma membrane showed protruding nanostructures, which is consistent with cortical actin protrusion. Proteins of the ERM family (ezrin, moesin, radixin), which play a fundamental role in tethering the membrane to the cellular membrane-proximal F-actin (MPA), can restrict local membrane protrusions and inhibit cancer cell migration[25]. This is nicely consistent with our Ezrin activation data showing that FKBP-Ezrin maintain a smooth membrane surface and inhibit high-crowding-exposed cells invasion (Fig. 8).

Abnormal changes in the cell membrane shape, including the bending and protrusion, affect the migration and invasion of cancer cell. Our findings and provides clues for potential clinical strategies targeting plasma membrane topography for early intervention of solid cancers provide a clue whether ERM proteins can be exploited for clinically therapeutic interventions aimed at normalizing cell membrane and cytoskeleton mechanics targeting deformed cells in the overcrowding tumor microenvironment.

`

MAIN FIGURES AND LEGENDS

Figure 1

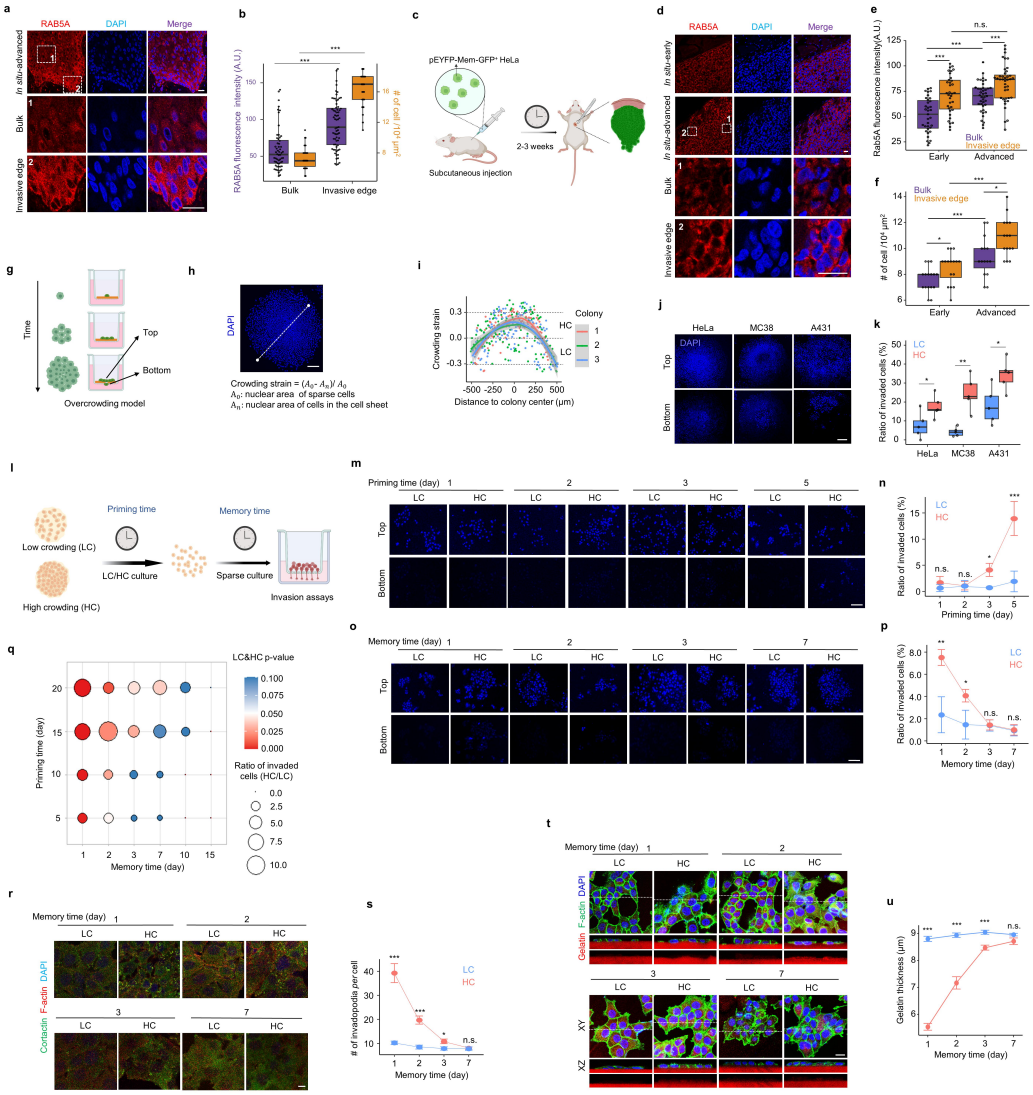

Figure 1. Overcrowding induces retentive invasiveness in cancer cells. (**a**) Immunofluorescence of in human skin cancer tissues. RAB5A (red), DAPI (blue). Scale bar: 20 μm. (**b**) Boxplot of nuclei number in per unit area (10e4 μm^2) and RAB5A fluorescence intensity from bulk and invasive edge focus. (**c**) Schematic diagram of subcutaneous nude mouse xenograft model using pEYFP-mem GFP+ HeLa cells. After 2 and 3 weeks of tumor growth, mice tissues were harvested and tumor architectures were analyzed for the indicated parameters. (**d**) Immunofluorescence of subcutaneous tumors from nude mouse xenograft. RAB5A (red), DAPI (blue). Scale bar: 20 μm. (**e**) Boxplot of RAB5A fluorescence intensity from bulk and invasive edge focus at in situ-early and in situ-advanced stages. (**f**) Boxplot of nuclei number in per unit area (10e4 μm^2) from bulk and invasive edge focus at in situ-early and in situ-advanced stages. (**g**) Schematic diagram of

`

overcrowding cell invasion model. (**h**) Quantitation of the individual cell nucleus area as crowding strain along the lines in panel. Scale bar: 200 μm. (**i**) The statistical analysis of the individual cell crowding strain along the lines in panel (g). The cell sheet was segmented into high crowding (HC: crowding strain from 0 to 0.3) and low crowding (LC: crowding strain from -0.3 to 0). (**j**) Transwell matrigel invasion assay of a growing monoclonal HeLa, MC38 and A431 cell sheets after culture for 14 days. Representative DAPI images of cells that accumulated on the top (uninvaded) and bottom (invaded) surface of the insert membranes. Scale bar: 200 μm. (**k**) The ratio of invaded cells in LC and HC of HeLa, MC38, and A431 cell sheets. (**l**) Schematic illustration of the experimental procedure to test the invasion of HeLa cells after priming time for LC and HC culture and memory time for sparse culture. (**m**) Transwell matrigel invasion assay of HeLa cells after experiencing LC and HC for 1, 2, 3, 5 days (priming time), and subsequently collected and transfered to transwell chamber for 48 hrs. Representative DAPI images of cells that accumulated on the top and bottom surface of the insert membranes. Scale bar: 100 μm. (**n**) The ratio of of invaded cells in LC and HC of HeLa cells in panel (m). (**o**) HeLa cells were grown dishes in HC or LC culture for 5 days, transfered to new dishes for 1, 2, 3, 7 days (memory time), and subsequently collected and transfered to transwell chamber for 48 hrs. (**p**) The ratio of of invaded cells in LC and HC of HeLa cells in panel (o). (**q**) The correlation graph between priming time and memory time in cell culture for invasion analysis. (**r**) HeLa cells were grown dishes in HC or LC culture for 5 days, transfered to matrigel-coated dishes for 1, 2, 3, 7 days. Representative XY slice image of cortactin distribution at the basal membrane in LC/HC groups. Scale bar: 10 μm. (**s**) Quantification of invadopodia number in per cell with corresponding memory time. (**t**) HeLa cells were grown dishes in HC or LC culture for 5 days, transfered to Cy5-conjugated gelatin hydrogels for 1, 2, 3, 7 days. Representative XY slice image of F-actin staining in LC/HC groups. Scale bar: 20 μm. (**u**) Quantification of correlation between Cy5-conjugated gelatin thickness located in per cell and its memory time. Data are presented as mean ± SEM; *$p < 0.05$, **$p < 0.01$, ***$p < 0.005$, not significant (n.s.); two-tailed unpaired t-test.

`

Figure 2

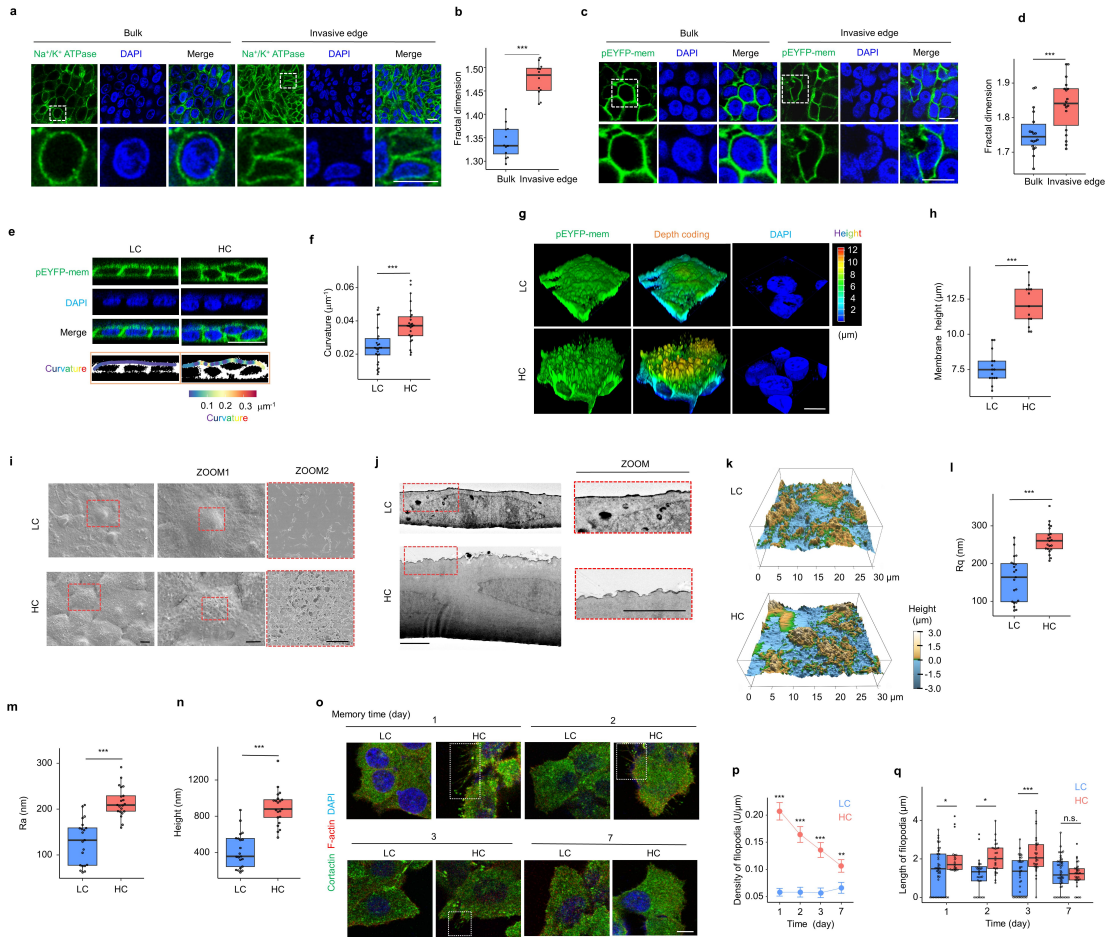

Figure 2. Overcrowding triggers nanocorrugated topographical transition of plasma membrane. (**a**) Representative XY slice image of sodium potassium ATPase (green) and nucleus (blue) in the low and high crowded regions of skin cancer tissues. Scale bar: 10 μm. (**b**) Quantitation of correlation between fractal dimension in per cell of human skin cancer tissue and its crowding strain. (**c**) Representative XY slice image of pEYFP (green) and nucleus (blue) from bulk and invasive edge focus of nude mouse xenograft. Scale bar: 10 μm. (**d**) Quantitation of correlation between fractal dimension in per cell from bulk and invasive edge focus of nude mouse xenograft. (**e**) Reconstructed XZ confocal images showing membrane curvature using ImageJ and plugin Kappa in LC and HC HeLa cells expressing membrane-EYFP. Scale bar: 20 μm. (**f**) Quantitation of membrane curvature values in LC and HC HeLa cells. (**g**) Confocal 3D reconstruction of the apical membrane of LC and HC HeLa cells expressing membrane-EYFP. Scale bar: 10 μm. (**h**) Quantitation of membrane height in LC and HC HeLa cells. (**i**) Scanning electron microscopy (SEM) images of cellular membrane in the cells experiencing different crowding strain. Scale bar: 10 and 5 μm. (**j**) Transmission Electron Microscope (TEM) images focusing on the apical plasma membrane reveal the presence of membrane bending in the range of 100 – 500 nm. Scale bar: 5 μm. (**k**) The topographic images of HeLa cells by AFM

show the height distribution of the membrane with the size of 30 μm × 30 μm. For low crowding cells, the surface of membrane was relatively flat and no pore-like structures were detected. More protruding structures can be observed for high crowding cells. (**l-n**) Root-mean-squared roughness (Rq), average roughness (Ra), and height distribution were analyzed from 3 × 3 μm frame ultrastructure images of HeLa cells by AFM. (**o**) Representative XY slice image of cortactin distribution in HeLa cells after LC/HC culture for 5 days and sparse culture for 1,2,3,7 days. Scale bar: 10 μm. (**p**) Quantification of filopodia density in per cell with corresponding memory time in panel (o). (**q**) Quantification of filopodia length in per cell with corresponding memory time in panel (o). Data are presented as mean ± SEM; *$p < 0.05$, **$p < 0.01$, ***$p < 0.005$; two-tailed unpaired t-test.

`

Figure 3

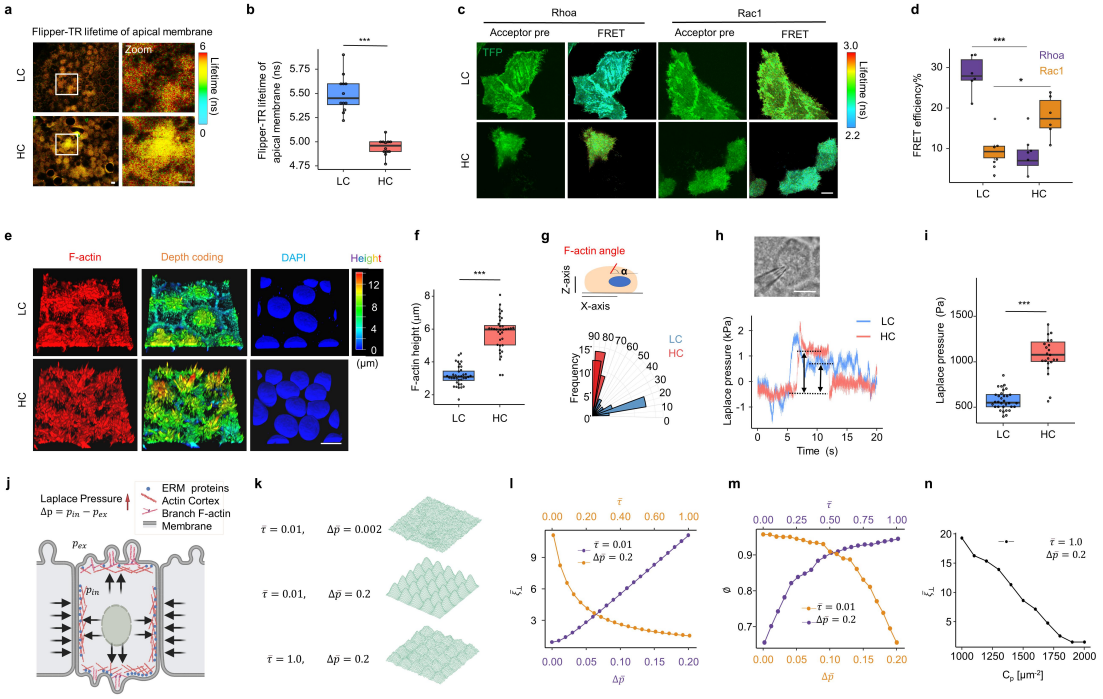

Figure 3. Overcrowding triggers nanocorrugated topographical transition of plasma membrane by increasing Laplace pressure. (**a**) Representative FLIM images of Flipper-TR lifetime values to analyze apical plasma membrane tension in LC and HC crowding cells. Color scale from 0 to 6 ns. Scale bars: 10 μm. (**b**) Quantification of the average lifetime of Flipper-TR from full images. Data are presented as boxplot. (**c**) FRET analysis on LC and HC HeLa cells transduced with a lentiviral construct expressing the RhoA or Rac1 biosensor. Representative confocal images of transduced cells before photobleaching (acceptor pre) are shown. Representative FLIM images of photobleached at the apical region of cells are shown. The colored scale represents the color range of FRET efficiency. Scale bar: 10 μm. (**d**) Quantitation of the fluorescence increase (% FRET efficiency) of RhoA and Rac1 upon photobleaching at the apical region of different crowding cells. Data are presented as boxplot. (**e**) Confocal 3D reconstruction of the apical membrane of LC and HC HeLa cells fixed and stained for F-actin. Scale bar: 10 μm. (**f**) Quantification of the average height of F-actin from the apical membrane in LC and HC cells. (**g**) Actin angle distribution data for cells experiencing LC and HC conditions displayed as a rose plot in which the absolute value of the angles was compared. (**h**) Quantifying Laplace pressure in low and high crowding HeLa cells using a micropressure probe. The baseline reading is close to zero when the microelectrode is not in contact with the cells. A transient pressure spike is recorded as the tip of the microelectrode penetrates the membrane. This is followed by a stable reading for about 5-10 s, before some potential leaks occur, which may cause a gradual drop in the reading with time. Scale bar: 10 μm. (**i**) Quantification of the Laplace pressure of cells experiencing

`

LC or HC. (**j**) Schematic representing how the Laplace pressure controls the distribution and size of cell membrane protrusion accompanied by an increase in Laplace pressure due to the cellular squeeze of each other. (**k**) Snapshot from Monte Carlo simulations of cell membrane surface morphology with different lateral tension $\bar{\tau} = \tau a^2 / \kappa$ and pressure difference $\Delta\bar{p} = \Delta p a^3 \left(\kappa k_{\mathrm{B}} T\right)^{-1/2}$ as indicated in each figure. (**l**) The rescaled roughness $\bar{\xi}_{\perp} = \xi_{\perp} \left(\kappa / k_{\mathrm{B}} T\right)^{1/2} / a$ as a function of lateral tension and pressure difference. (**m**) The number of proteins that bound to the cytoskeleton as a function of pressure difference and lateral tension. (**n**) The rescaled roughness as a function of the density of proteins that bound to the cytoskeleton. Data are presented as *p < 0.05, **p < 0.01， ***p < 0.005; two-tailed unpaired t-test.

`

Figure 4

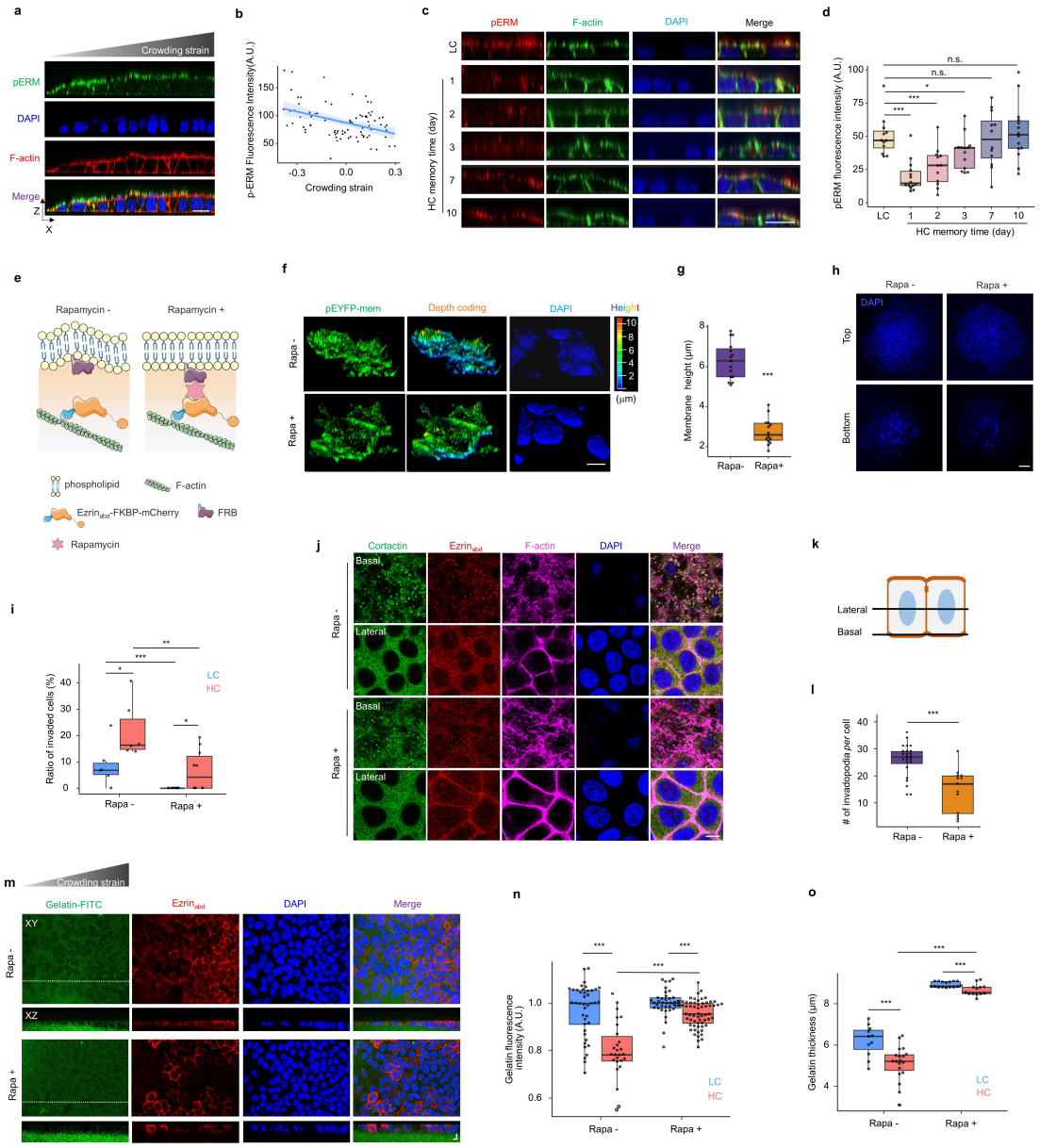

Figure 4. Suppressing nanocorrugated topographical transition of plasma membrane abrogates overcrowding-induced cancer cell invasion. (**a**) Reconstructed XZ confocal images show apical localization of pERM (green) in different crowding regions of monoclonal HeLa cell sheets. Scale bar: 20 μm. (**b**) Quantification of the pERM fluorescence intensity per cell with corresponding crowding strain. (**c**) Reconstructed XZ confocal images show apical localization of pERM (green) in HeLa cells after LC/HC culture for 5 days and sparse culture for 1,2,3,7,10 days. Scale bar: 20 μm. (**d**) Quantification of the pERM fluorescence intensity per cell with corresponding memory time. (**e**) Schematic for a Ezrin$_{abd}$-FKBP-FRB construct to acutely increase membrane proximal F-actin because of recruitment of the Ezrin$_{abd}$ to the plasma membrane after rapamycin treatment. (**f**)

`

Confocal 3D reconstruction of the apical membrane of FKBP-Ezrin$_{abd}$T567D^{+} HeLa-pEYFP-mem cells treated with rapamycin or vehicle. Scale bar: 10 μm. (**g**) Quantification of the average height of membrane from the apical membrane in control and rapamycin treated cells. (**h**) Transwell matrigel invasion assay of FKBP-Ezrin$_{abd}$T567D^{+} HeLa cell sheets after treatment with rapamycin or vehicle. Representative DAPI images of cells that accumulated on the top (uninvaded) and bottom (invaded) surface of the insert membranes. Scale bar: 100 μm. (**i**) Ratio of invaded cells in FKBP-Ezrin$_{abd}$T567D^{+} HeLa cell sheets treated with rapamycin or vehicle in panel (h). (**j**) Representative XY slice image of cortactin and F-actin staining in FKBP-Ezrin$_{abd}$T567D^{+} HeLa cell sheets treated with rapamycin or vehicle. Scale bar: 10 μm. (**k**) Schematic diagram of apical, lateral and basal cross-sections in HeLa cell sheets. (**l**) Quantification of invadopodia density per cell in control and rapamycin groups in panel (j). (**m**) FKBP-Ezrin$_{abd}$T567D^{+} HeLa cells were plated on FITC-conjugated gelatin hydrogels. Representative XY and XZ slice image of gelatin-FITC and Ezrin$_{abd}$ in HeLa cell sheet after rapamycin treatment. Scale bar: 10 μm. (**n,o**) Quantification of correlation between Cy5-conjugated gelatin fluorescence intensity and thickness located per cell in control and rapamycin groups in panel (m). Data are presented as *$p < 0.05$, **$p < 0.01$， ***$p < 0.005$; two-tailed unpaired t-test.

`

Figure 5

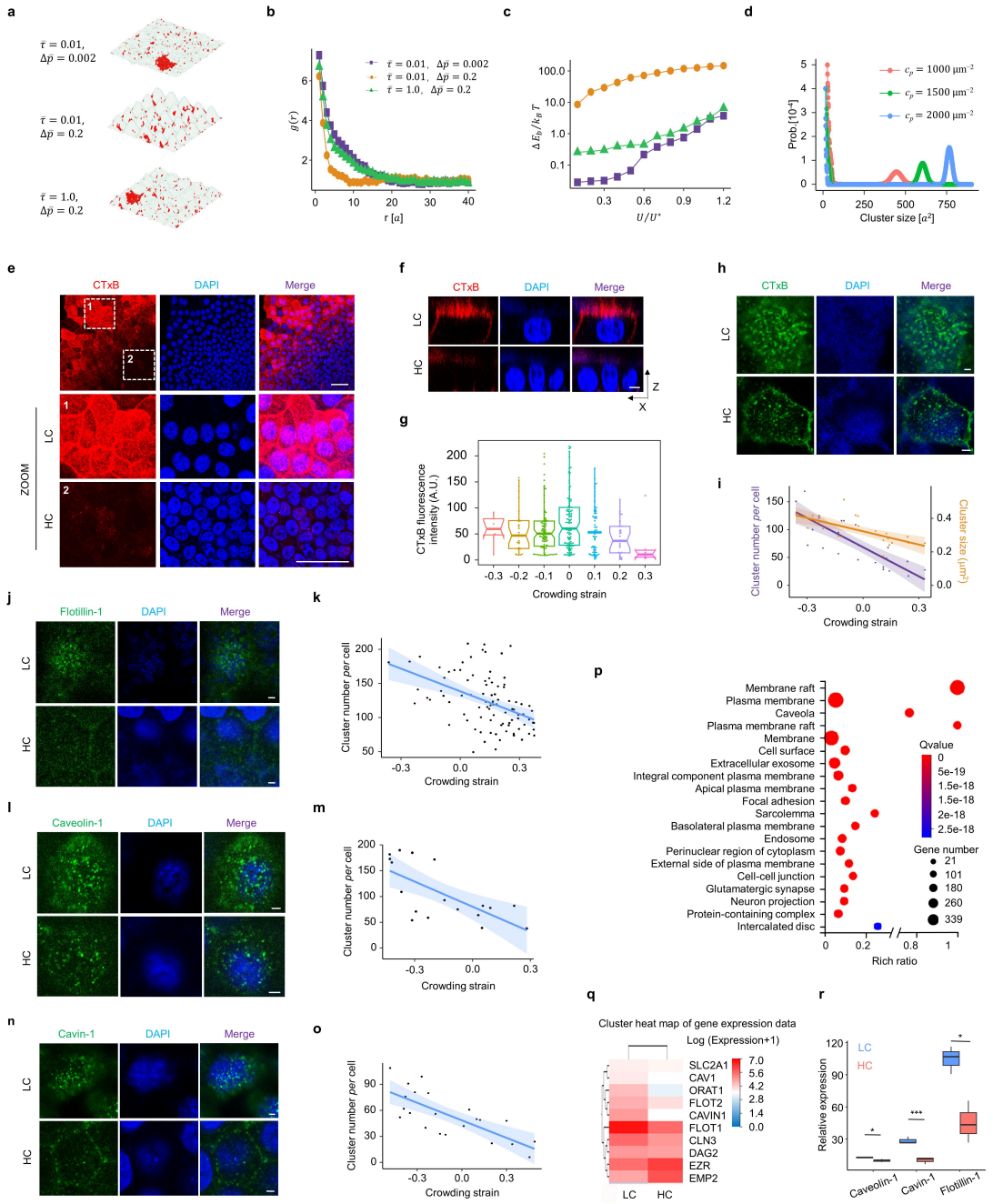

Figure 5. Overcrowding-induced nanocorrugated topographical transition of plasma membrane disrupts lipid raft-like domains organization. (**a**) Snapshot from Monte Carlo simulations of lipid rafts distribution for different lateral tension and pressure difference as indicated in each figure. (**b**) Pair distribution function g (r) of lipid rafts as a function of the distance r for different lateral tension and pressure difference as indicated in this figure. (**c**) The change of bending energy as a function of the raft-raft contact energy. The color code is as in panel (b). (**d**) Size distributions of raft clusters for different area concentrations of proteins that bound to the

cytoskeleton in membrane. (**e**) Representative XY confocal images showing immunofluorescence staining for CTB in different crowding regions of monoclonal HeLa cell sheet. Scale bar: 50 μm. (**f**) Reconstructed XZ confocal images show apical localization of CTxB in different crowding regions of monoclonal HeLa cell sheets. Scale bar: 5 μm. (**g**) Quantitation of correlation between CTxB fluorescence intensity per cell and its crowding strain. (**h**) Representative XY confocal images showing immunostaining for CTxB at the apical membrane of different crowding cells. Scale bar: 2 μm. (**i**) Quantitation of CTxB fluorescence intensity per cell and its crowding strain. (**j**) Representative XY confocal images showing immunostaining for Flotillin-1 at the apical membrane of different crowding cells. Scale bar: 2 μm. (**k**) Quantitation of Flotillin-1 number per cell and its crowding strain. (**l**) Representative XY confocal images showing immunostaining for Caveolin-1 at the apical membrane of different crowding cells. Scale bar: 2 μm. (**m**) Quantitation of correlation between Caveolin-1 number per cell and its crowding strain. (**n**) Representative XY confocal images showing immunostaining for Cavin-1 at the apical membrane of different crowding cells. Scale bar: 2 μm. (**o**) Quantitation of correlation between Cavin-1 number per cell and its crowding strain. **(p)** Go enrichment analysis of deferentially expressed genes (DEGs) from from different crowding regions of monoclonal HeLa cell sheets by a wide-mouth pipette for SMART seq II. Q value<0.05. (**q**) Heat map of the deferentially expressed genes in low and high crowding cells. (**r**) Boxplot of related gene expression of Caveolin-1, Cavin-1, and Flotillin-1 in low and high crowding HeLa cells as determined by SMART seq II. Data are presented as *$p < 0.05$, **$p < 0.01$，***$p < 0.005$; two-tailed unpaired t-test.

`

Figure 6

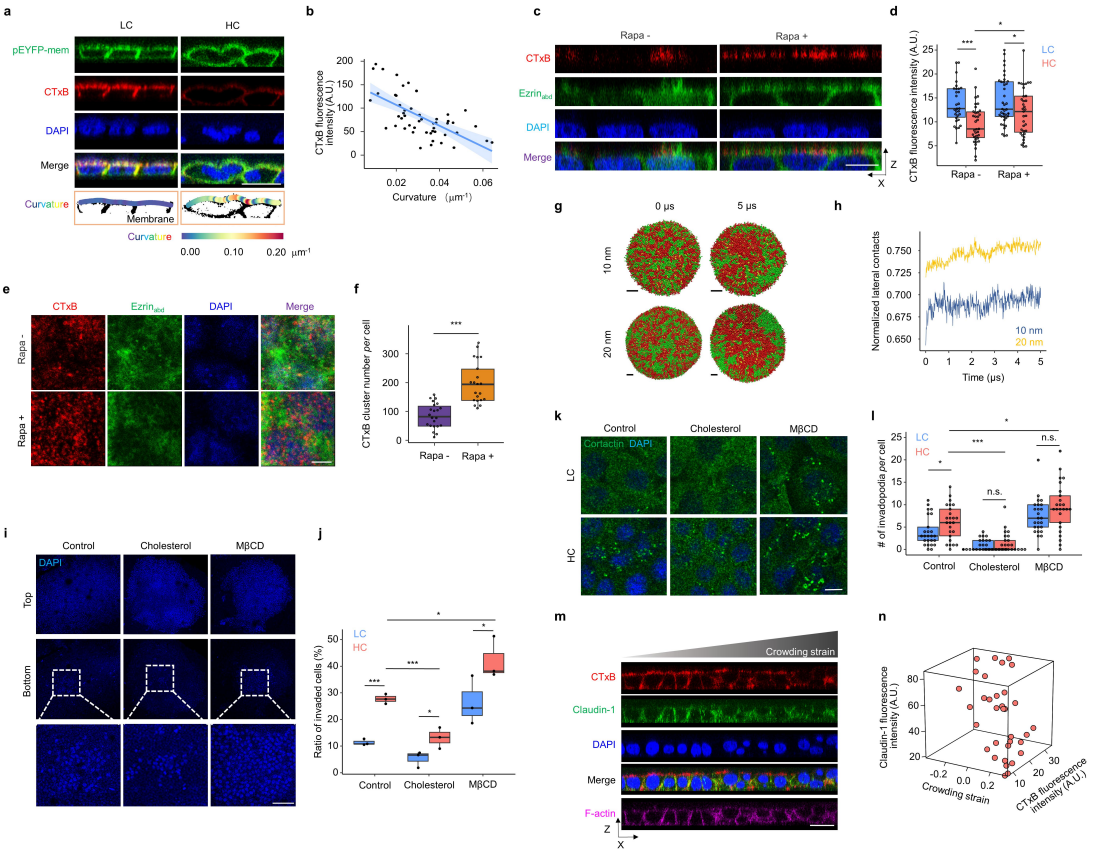

Figure 6 Overcrowding-triggered nanocorrugated topographical transition of plasma membrane promotes cancer cell invasion by disrupting lipid raft-like domains organization. (**a**) Reconstructed XZ confocal images showing CTxB level and membrane curvature using ImageJ and plugin Kappa in low and high crowding HeLa cells expressing membrane-EYFP. Scale bar: 20 μm. (**b**) Quantitation of correlation between CTxB fluorescence intensity and membrane curvature in different crowding HeLa-pEYFP-mem cells. (**c**) Reconstructed XZ confocal images showing CTxB fluorescence intensity in FKBP-Ezrin$_{abd}$T567D^{+} HeLa cell sheets treated with rapamycin or vehicle. Scale bar: 10 μm. (**d**) Quantitation of correlation between CTxB fluorescence intensity in LC and HC cells treated with rapamycin or vehicle. (**e**) Representative XY confocal images showing immunostaining for CTxB at the apical membrane of FKBP-Ezrin$_{abd}$T567D^{+} HeLa cell sheets treated with rapamycin or vehicle. Scale bar: 5 μm. (**f**) Quantitation of correlation between the number of CTxB cluster in per cell treated with rapamycin or vehicle. (**g**) Snapshots of DPPC (red) / DUPC (green) / CHOL (yellow) liposomes with different inner radius and at different time. Scale bar: 4 nm. (**h**) Time evolution of normalized lateral contacts of DUPC lipids for different systems. (**i**) Representative XY slice images of cholesterol and MβCD-treated HeLa cell sheets by transwell invasion assay. Scale bar: 100 μm. (**j**) Quantification of invaded cell number in cholesterol and MβCD-treated HeLa cell sheets above. (**k**) Representative XY slice image of cortactin in LC and HC regions of

`

cholesterol and MβCD-treated HeLa cell sheets. Scale bar: 10 μm. (**l**) Quantification of invadopodia density in per cell in panel (k). (**m**) Reconstructed XZ confocal images show the localization of CTxB and Claudin-1 in HeLa cell sheet with different crowding strain. Size bars: 20 μm. **(n)** Quantitation of correlation between Claudin-1 fluorescence intensity and CTxB level in different crowding cells. Data are presented as *$p < 0.05$, **$p < 0.01$， ***$p < 0.005$; two-tailed unpaired t-test.

`

Figure 7

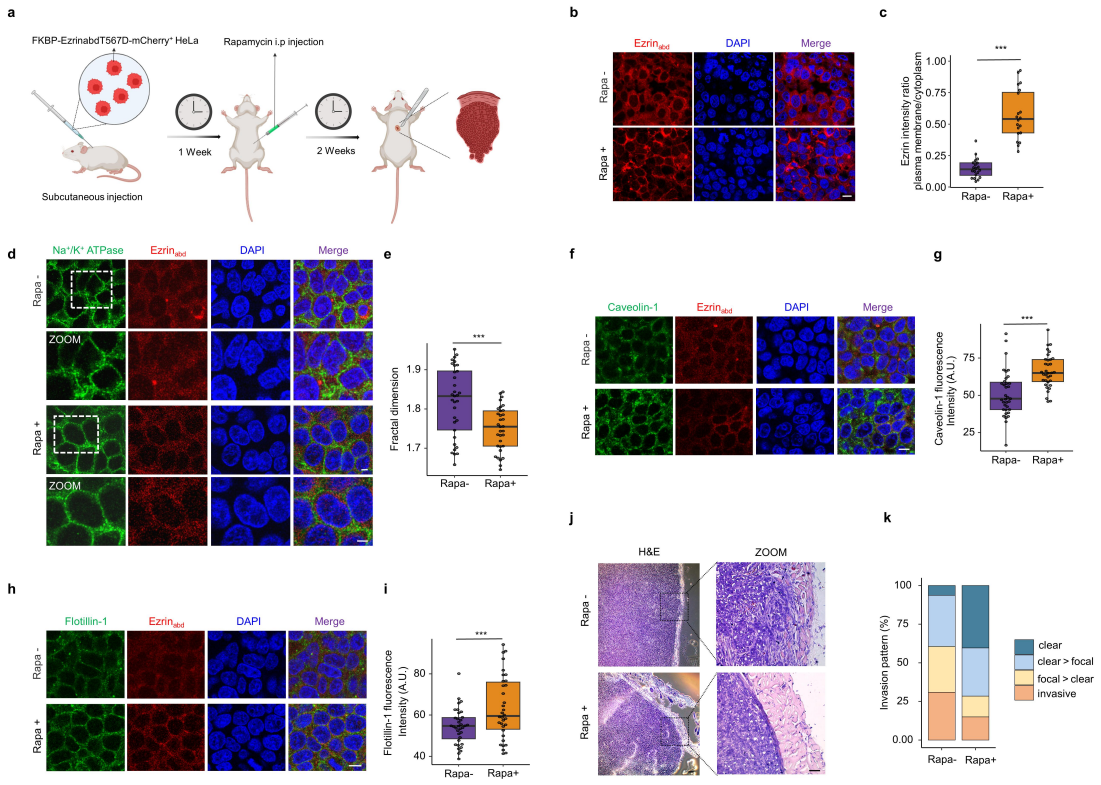

Figure 7. Suppressing nanocorrugated topographical transition of plasma membrane resists to tumor invasion in a xenograft mouse model. (**a**) Schematic diagram of subcutaneous nude mouse xenograft model using FKBP-Ezrin$_{abd}$T567D HeLa cells. After 1 week of tumor growth, mice was treated with rapamycin or vehicle via i.p. three times per week. Tissues were harvested and tumour architectures were analyzed for the indicated parameters. (**b**) Immunofluorescence analysis of Ezrin$_{abd}$T567D location (red) in mouse xenografts treated with rapamycin or vehicle above. (**c**) Quantification of Ezrin$_{abd}$T567D distribution in tumor cells of mouse xenografts. (**d**) Representative XY slice image of sodium potassium ATPase (green) and Ezrin$_{abd}$T567D location (red) in mouse xenografts treated with rapamycin or vehicle. Scale bar: 5 µm. (**e**) Quantitation of correlation between fractal dimension in per tumor cell in mouse xenografts. (**f**) Immunofluorescence analysis of Caveolin-1 (green) in mouse xenografts treated with rapamycin or vehicle above. Scale bar: 10 µm. (**g**) Quantification of Caveolin-1 fluorescence intensity in tumor cells of mouse xenografts. (**h**) Immunofluorescence analysis of Flotillin-1 (green) in mouse xenografts treated with rapamycin or vehicle above. Scale bar: 10 µm. (**i**) Quantification of Flotillin-1 fluorescence intensity in tumor cells of mouse xenografts. (**j**) Representative images of rapamycin or vehicle treated mice subcutaneous xenografts stained for HE. Overview images, scale bar: 200 µm; detailed images, scale bar: 50 µm. (**k**) Invasion pattern of mice subcutaneous xenografts treated with rapamycin or vehicle. Invasion was classifed as "clear" (distinct border between muscle and tumor), "clear>focal" (more clear borders than areas with focal invasions),

`

“focal>clear” (more focal invasions than clear borders), or “invasive” (no clear borders). Percentages of each category are given. Only samples with sufficient surrounding muscle tissue were evaluated. Data are presented as *$p < 0.05$, **$p < 0.01$， ***$p < 0.005$; two-tailed unpaired t-test.

`

Figure 8

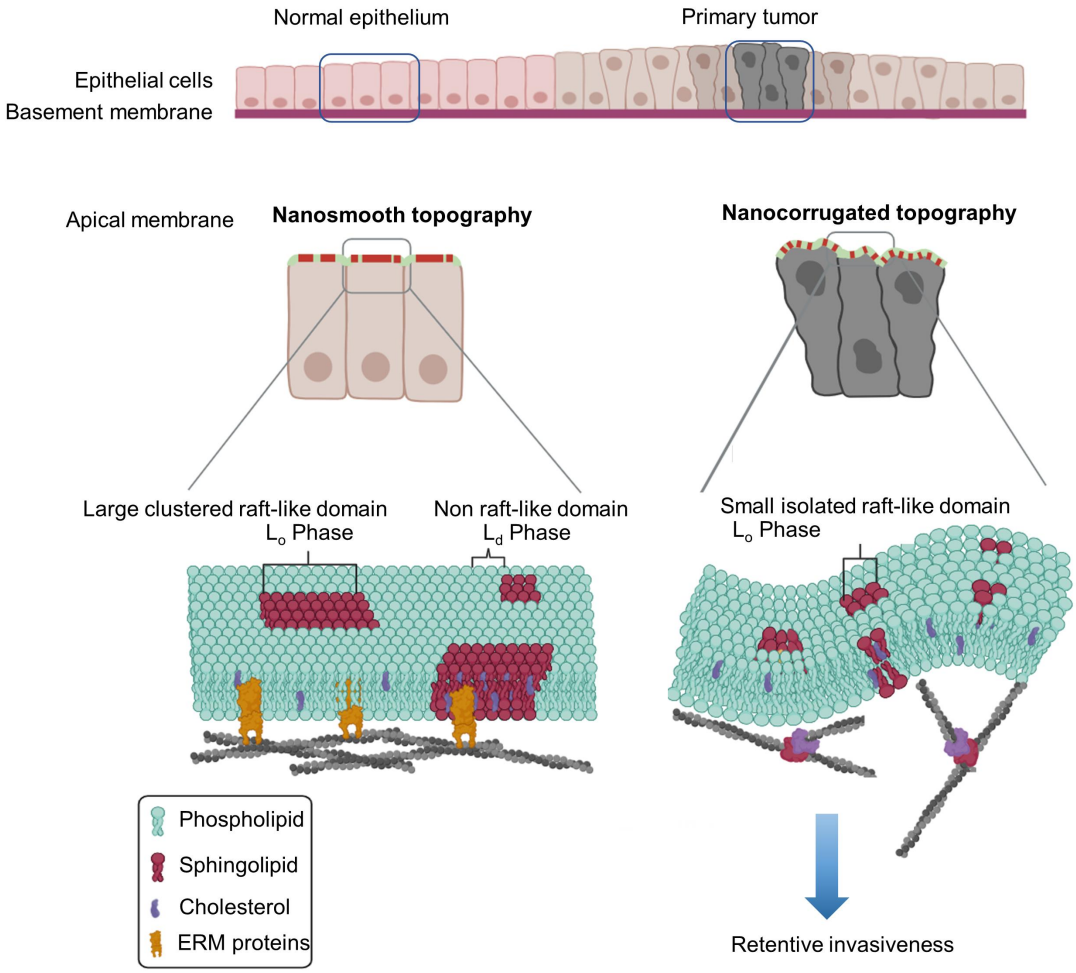

Figure 8. Schematic of the control of the reconstitution of Lo domains by topographic structures in the apical membrane of normal epithelium and primary tumor experiencing different crowding strain. The supported membrane consists of L_d phase containing unsaturated phospholipids and the L_o phase that are raft domain by association of sphingolipid and cholesterol molecules. Large clustered raft domains are located in nanosmooth topography experiencing low crowding, which maintain a flat plasma membrane sustained by membrane-to-cortex attachment. Small isolated raft domains are confined in a region with nanocorrugated topography experiencing high crowding, which shows a plasma membrane protrusion pushed forward by Arp2/3 complex-dependent branched actin polymerization.

`

EXPERIMENTAL MODEL AND SUBJECT DETAILS

Mice

SPF male BALB/c nude mice aged 3-4 weeks and weighing 16-18 g were purchased from Vital River Laboratory Animal Technology Co., Ltd. Mice were bred and reared in the animal facility of Tsinghua University at 22 °C with a 12-hour light/dark cycle (lighting time 7:00-19:00). Food and water are freely available. All animal studies were conducted under the guidance of the Animal Care and Utilization Committee (IACUC) of Tsinghua University. According to the National Institutes of Health "Animal Ethical Use Guidelines", the experimental procedure has been approved by the Laboratory Animal Care and Use Management Committee of Tsinghua University and the Beijing Municipal Science and Technology Commission (SYXK-2019-0044).

Human Tissues

Primary breast cancer, skin cancer and cervix cancer samples (paraffin sections) were obtained from patients who had undergone breast surgery at the Dezhou Second People's Hospital. The cases were classified according to the World Health Organization classification criteria of the tumors of the breast. The samples were obtained with the patients' consent following approval by the Institutional Committee for the Welfare of Human Subjects.

Cancer Cell Lines

HeLa, A431, and MC38 cells were cultured in Dulbecco's modified eagle medium

`

(DMEM) medium (containing with 4.5 g/L glucose, L-glutamine and sodium pyruvate) supplemented with 10% fetal bovine serum (FBS; Life technologies, CA, USA), and 100 IU/mg penicillin – streptomycin (Life technologies, CA, USA), and 1% (v/v) non-essential amino acids (NEAA; Life technologies, CA, USA).

METHOD DETAILS

Plasmids Construction and Transfection

Cells were transiently transfected with plasmid DNA (pEF1-Lifeact-mCherry, pEYFP-membrane pTriEx4-Rac1-2G and pTriEx-RhoA-2G) using Lipofectamine 2000 (PN: 11668030, Invitrogen), according to the manufacturer's protocol. pTriEx4-Rac1-2G and pTriEx-RhoA-2G were a gift from Olivier Pertz (Addgene plasmid no. 66110 and 40176). Rac1-2G-control and RhoA-2G-control were constructed by deleting coding sequence of acceptor Venus. C1-mCitrine-FKBP-EZRabd(t567D), pCAG-Lyn11-FRB and YFP-FKBP were a gift from Tobias Meyer (Addgene plasmid no. 155227, 155228 and 20175). pLV[Exp]-Puro-CMV>mCherry/FKBP-EZRabd(t567d),pLV[Exp]-Puro-CMV>mCherry/FKBP and pLV[Exp]-Puro-EF1A>Lyn-FRB-HA were constructed by VectorBuilder.

Drug Treatments

Pharmacological inhibitors and chemical compounds were used at the following concentrations: 100 μM Cholesterol (Merck, #57-88-5), 100 μM MβCD (lipid raft

`

inhibitor; Merck, #128446-36-6). Rapamycin (MCE, #53123-88-9). Rapamycin was dissolved in DMSO for treatment in cells (5 μM) and dissolved in 5.2% polyethylene glycol and 5.2%Tween-80 for treatment in mice (2.0 mg/kg)

Subcutaneous Murine Xenograft Model

Cervical tumors were established by subcutaneous inoculation of $5X10^6$ HeLa cells into the suprascapular region of 6-week-old nude mice (6 per group). When tumors reached 100–200 mm^3 after 1 week, mice were randomly assigned to receive intraperitoneal injection of vehicle (0.25 % polyethylene glycol, 0.25 % tween) or rapamycin (2 mg/kg) every other day. Tumors were measured weekly using calipers and volume was calculated as (length X $width^2$)/ 2. Mice were killed after 2 weeks of treatment, and tumors were excised and fixed with 4% paraformaldehyde.

Immunofluorescence and Histological Analysis

Cells grown on glass bottom or confocal dishes were fixed with 4% paraformaldehyde, permeabilized with 0.1% Triton X-100 for 5 min. Cells were incubated with primary antibodies at the optimal concentrations (according to the manufacturer' s instructions) at 4 °C overnight. Following three washes with PBS, samples were incubated with the appropriate secondary antibodies: 488/568/633 immunoglobulin G (IgG; H+L) and/or Alexa Flour 568/647 phalloidin (Invitrogen) for 1 h at room temperature. Samples were again washed three times with PBS and mounted with 4',6-diamidino-2-phenylindole (DAPI, Invitrogen) for 10 min at room temperature.

`

Confocal images were taken on the Leica microscope Experiments were replicated at least three times. Acquisition of fluorescent images were carried out using a Leica TCS SP8 AOBS Confocal laser-scanning microscope equipped with a 10×, 40×, or 63× objective (Leica, Germany).

Prior to embedding in paraffin, human or mouse tissues were fixed in 4% paraformaldehyde in PBS and dehydrated. For histological analysis, 6 μm sections were cut and stained with Hematoxylin and Eosin. For immunofluorescence analysis, 6 μm sections were incubated for 20 min in 10 mM sodium citrate buffer, pH 6.0 at 90 °C to retrieve antigens on paraffin-embedded tissue samples. After 1h incubation in 5% fetal calf serum, sections were incubated overnight with diluted primary antibodies, washed and further incubated for 2 h at room temperature with appropriate secondary antibodies. Nuclei were stained with DAPI for 10 min at room temperature. Confocal images were taken on the Leica microscope equipped with a 10×, 40×, or 63× objective. Experiments were replicated at least three times.

Cholera Toxin Subunit B (CTxB) staining

HeLa cells were grown on 35 mm confocal dishes and cultured for 12 days. The cells were then rinsed with cold Hank's balanced salt solution (HBSS)+0.5% BSA and incubated with 0.5 μg/mL CFTM 488A or 633 conjugated CT-B in cold HBSS+0.5% BSA and incubate at 4°C for 30 minutes in the dark. Cells were washed five times with cold HBSS+0.5% BSA and fixed in 4% paraformaldehyde in PBS for 15 minutes

`

at room temperature. Nuclei were stained with DAPI for 10 min at room temperature.

Transwell Invasion and Migration Assays

For the transwell invasion assay, briefly, 5-10 cells in 200 μL 10% FBS DMEM were reseeded into the upper chamber of a 24-well transwell of 8 μm pore size (Corning Inc., Corning, NY, USA) with coated-Matrigel (BD Bioscience, San Jose, CA, USA), and 600 μL medium with 10% FBS was loaded into the well below. After culture for 12 days, the upper chamber was replaced with serum-free medium and later incubated at 37 °C for 48 h. Transwell insert membranes were fixed with 4% paraformaldehyde and stained with DAPI. For the Transwell migration assay, all procedures were similar but without the incubation of Matrigel. The percentage of migrating and invading cells through the filter were imaged under a Leica SP8 Confocal microscope, and measured using the ImageJ software.

Cy5-GelMA degradation assay

Gelatin methacryloyl (GelMA, EFL-GM-RF-90, China), lithium phenyl-2, 4, 6-trimethylbenzoylphosphinate (LAP), and a blue light source (3 W, 405 nm) were purchased from Engineering for Life, Suzhou, China. GelMA-Cy5 was dissolved in PBS at 30% (w/v) containing 0.25% (w/v) LAP. The mixture was transferred to a glass slide and exposed to blue light irradiation for 90 s to crosslink the GelMA. Then the prepared hydrogels were rinsed with PBS three times, and then single cell was seeded on hydrogels in 24-well plates and cultured for 14 days. Cells were fixed with

`

4% paraformaldehyde at room temperature for 15 min and washed three times with PBS. The sample was incubated in 0.1% Triton X-100 for 10 min. Subsequently, the samples were stained for actin with phalloidin for 60 min and stained for nuclei with DAPI for 10 min.

SMART-seq Ⅱ analysis

HeLa cells were seeded on 10 cm dish and cultured for 12 days. Low and high crowding regions from three cell sheets were collected by the mouth pipette and each region contains about 100 cells. The samples were sent to the Beijing Genomics Institute (BGI, China) for RNA sequencing performed on the BGISEQ-500 platform. The data was analyzed using Dr. Tom system multi-omics interactive system (BGI, China). Q-value was obtained by false discovery rate (FDR) correction of the P-value. Differentially expressed genes (DEGs) ($Q \leq 0.05$, $|\log2FC| \geq 1$) were analyzed by DEseq2 software. Gene Ontology (GO) cellular components ($Q \leq 0.05$) enrichment analysis and hierarchical clustered heat map visualization of gene expression patterns were performed using Dr. Tom and results with $Q \leq 0.05$ were considered statistically significant.

Atomic Force Microscopy (AFM)

HeLa cells were grown on 35 mm confocal dishes and cultured for 12 days. Cell samples were fixed directly by 4% paraformaldehyde, after washing cells with PBS to remove potential impurities on the cell surface, and then kept in PBS. AFM

`

experiment was performed in PBS buffer solution at room temperature in PeakForce Tapping mode by scanning probe microscope Asylum MFP-3D-SA (Asylum Research, USA). A PeakForce qp-BioAC probe probe (nominal spring constant 0.06-0.18 N/m, Nanosensors, Neuchatel, Switzerland) was used to image the cell surface. The material properties were as follows: scan size of 30 μm, scan rate of 0.1 Hz, set point of 162.21 mV, integral gain of 611.37, drive amplitude of 2 V. All images were taken at a resolution of 256×256 pixels. The scan area depended on the size of the HeLa cell and ranged from 30×30~50×50 μm^2. Image processing and data analysis were performed by the Asylum MFP-3D-SA software.

Focused ion beam and scanning electron microscopy analyses

Sample fixation of micropatterned HeLa cells was performed at room temperature for 15 min using a 2.5% v/v glutaraldehyde (Electron Microscopy Sciences) solution in PB buffer. After washing the samples three times with PB buffer, the samples were osmicated with 1%osmium tetroxide/1.5% potassium ferricyanide in distilled water for 30min. Then, samples were washed three times with distilled water and then dehydrated through a graded ethanol series. After dehydration, samples were infiltrated with Pon 812 Resin (SPI) by incubating the samples in a diluted series of ethanol- Pon 812 at a 1:1, 1:2 and 1:3 ratio for 1h each, and then overnight in pure resin. After that, pure resin was changed once in the first 1h and then incubated in an oven at 60 ° C for 48 h. 70 nm sections were cut by ultramicrotome (Leica EM UC7) then stained by uranyl acetate (UA) and lead citrate. Then imaged by TEM. To

`

visualize the surface of the cell, the resin covering the cell was removed by acetone, then cells filled by resin were polymerized at 60 ° C for 48h. 10nm gold were coated before imaged by SEM. After that, resin was added again.70 nm Cross section of the cells were cut for TEM

Laplace pressure calculation

Laplace pressure measurements were conducted using the 900A micro pressure system (WPI) based on the servo-null method, following the manufacturer's instructions. A microelectrode was created from a glass capillary (0.75 mm inner diameter/1.0 mm outer diameter) using a micropipette puller (PC-100, Narishige). The one-stage pull mode was employed with the following settings: Heat 50V, Weights: 250 g. Prior to measurement, the microelectrode was calibrated using the provided calibration chamber and a pressure source. The microelectrode was filled with a 1M NaCl solution, while the calibration chamber contained a 0.1M NaCl solution.

To perform the measurements, the microelectrode was mounted to a piezo-driven xyz micromanipulator (SN-PCZ-50R, WPI) located in an environmental chamber (37 ° C, 5% CO2). A four-channel AD converter was used to record the pressure signal. The microelectrode tip was inserted into the cells at a 45-degree angle and then slightly retracted to release compression on the cells. This position was maintained for at least 10 seconds. The Laplace pressure was determined as the average pressure over this 10-second period.

`

Membrane Tension Measurements

Cell membrane tension was measured with Flipper-TR fluorescent tension probe (SC020, Cytoskeleton, Inc.). HeLa cells were cultured on the gelatin-coated 35 mm confocal dishes for 12 days until the cell sheet was formed. Cells were treated with 1 mM Flipper-TR at 37 °C for 15 minutes to achieve appropriate labeling prior to imaging. The fluorescence lifetime of Flipper-TR was measured by using an Olympus fluorescence lifetime imaging microscopy (FLIM, FV-1200, Japan). Excitation was performed using a pulsed 488-nm laser operating at 40 MHz, and the emission signal was collected through a 550-650-nm bandpass filter using a HyD SMD detector. Lifetimes of Flipper-TR were extracted from FLIM images using SymPhoTime 64 software (PicoQuant). We selected full images instead of choosing a region of interest.

Fluorescence Resonance Energy Transfer (FRET)

HeLa cells were cultured on the gelatin-coated 35 mm confocal dishes for 12 days and transfected with genetically encoded biosensors expressing RhoGTPases Rac1-2G-control, Rac1-2G, RhoA-2G or RhoA-2G-control. After 48 hours, acquisition of fluorescent images and FRET experiments were carried out using an Olympus FV-1200 Confocal laser-scanning microscope. Argon laser lines 458 nm and 514 nm were used to excite mTFP1 and mVenus fluorophores, which represent the donor and the acceptor, respectively. For proper image recording, a HyD SMD

`

detector were employed by gating a spectral acquisition window of 486-502 nm for the donor and 524-600 nm for the acceptor. FRET analysis was performed using SymPhoTime 64 software (PicoQuant) and FRET efficiency was calculated: 1-τdonor, Rac1 or Rhoa-2G /τdonor, Rac1 or Rhoa-2G-control.

Molecular Dynamics (MD) Simulations

In this work, CHARMM-GUI webserver[51], Martini coarse-grained force field[52] and GROMACS software[53] (version 2019.6) were used to perform all MD simulations to capture the phase separation processes of three-component lipid vesicles with different radius (10 nm and 20 nm). 1,2-dipalmitoyl-sn-glycero-3-phosphocholine (DPPC),1,2-dilinoleoyl-sn-glycero-3-phosphocholine (DUPC), and cholesterol (CHOL) with the molar ratio of 5:3:2 was adapted to construct the lipid vesicles for studying the kinetics of model lipid rafts[54,55]. For all simulations, a standard 1.2 nm cutoff was applied for van der Waals interactions, where the LJ potential was shifted to zero smoothly from 0.9 to 1.2 nm to reduce the cutoff noise. For columbic potential, a 1.2 nm cutoff was used for short-range electrostatic interactions while shifting to zero from 0 to 1.2 nm smoothly. The neighbor list for nonbonded interactions was updated every 10 steps with a cut-off of 1.2 nm. Periodic boundary conditions were applied in all three dimensions. All simulations were run for 5 μs with the time step of 20 fs under the isothermal-isobaric (NPT) ensemble. Snapshots and movies were rendered by VMD[56].

`

Monte Carlo (MC) simulations

We consider a raft-containing multicomponent membrane interacting with cortical cytoskeleton *via* the transmembrane proteins. The membrane undergoes thermally-excited fluctuations and is subjected to both pressure and lateral tension. In our model, the cell membrane is represented by a two-dimensional surface which is discretized into square lattices with index i. The shapes of the cell membrane can be described in the Monge parameterization by its local heights h_i from a planar reference plane. The elastic deformations of the cell membrane are regulated by the membrane bending rigidity, membrane tension, as well as pressure acting on the membrane. The elastic energy of the cell membrane is then given by the discretized Helfrich Hamiltonian[57]

$$\mathrm{H}_{\mathrm{el}} = \sum_i \left[\frac{\kappa_i}{2a^2} \left(\nabla_{\mathrm{d}}^2 h_i \right)^2 + \frac{\tau}{2} \left(\nabla_{\mathrm{d}} h_i \right)^2 - \Delta p a^2 h_i \right] \tag{1}$$

where, in the bending rigidity term, κ_i is the bending rigidity of the cell membrane at lattice site i, $\nabla_{\mathrm{d}}^2 h_i$ is discretized Laplacian of the local membrane height h_i; in the tension term, τ is the lateral tension of the cell membrane, $\left(\nabla_{\mathrm{d}} h_i\right)^2$ describes the increase of membrane area per unit projected area; in the pressure term, $\Delta p = p_{\mathrm{in}} - p_{\mathrm{ex}}$ is the difference between Laplace pressure (p_{in}) and extracellular pressure (p_{ex}). In our study, the lattice size a set the length unit and is taken to be a = 5 nm to capture the complete spectrum of membrane shape fluctuations, and we vary the membrane tension and pressure difference up to a few mN/m and several thousand Pa, respectively, to systematically study the cell response.

By analogy to the lattice-gas-type models, a single square membrane patch can

`

accommodate one protein. Thus, the spatial distribution of transmembrane proteins in cell membrane is described by the binary variable n_i with values 0 or 1. n_i = 1 indicates the protein is present at membrane patch i, whereas n_i = 0 indicates the membrane patch i contains no protein. Neglecting the thermal shape fluctuations of the cytoskeleton, we use a rigid uniform square mesh framework with a pore size $20a$ = 100 nm and a filament diameter of $2a$ = 10 nm to resemble the crosslinked cytoskeletal networks beneath the cell membrane[58]. Similarly, the spatial distribution of cytoskeletal network is described by the binary variable m_i with values 0 or 1 indicating the absence or presence of the cytoskeleton underneath the membrane patch i. The transmembrane proteins can interact with the cytoskeletal network *via* a harmonic potential, and the total binding energy is given by[59,60]

$$\mathrm{H}_{\mathrm{in}} = \sum_i m_i n_i \left(-U_{\mathrm{b}} + \frac{1}{2} k l_i^2 \right) \theta \left(\frac{l_{\mathrm{b}}}{2} - \left| l_i - l_{\mathrm{p}} \right| \right) \tag{2}$$

Here, $U_{\mathrm{b}} > 0$ is the binding energy, l_i is local separation of membrane and cytoskeleton at site i, l_{b} is the binding range, l_{p} is the protein length, k is a control parameter that determines the width of the binding-distance distribution. The Heaviside step function $\theta(x)$ implies that a protein cannot bind to the cytoskeleton if they are separated beyond the binding range. Here, we choose $U_{\mathrm{b}} = 15 k_{\mathrm{B}} T$, $l_{\mathrm{b}} = 1.0\mathrm{nm}$, $l_{\mathrm{p}} = 15.0\mathrm{nm}$, $k = 2.0 k_{\mathrm{B}} T / \mathrm{nm}^2$. The area concentration of proteins is set to be 2000μm^2.

A single lipid raft occupies one membrane patch. The spatial distribution of lipid rafts is described by the binary variable w_i with values 0 or 1. w_i = 1 indicates that the membrane patch at site i is within the lipid rafts, while w_i = 0 means that the

`

membrane patch at site i is a part of surrounding membrane matrix. The lipid rafts undergo dynamic fission into smaller ones or merging to form larger domains. To capture the coalescence propensity of lipid rafts partially due to their hydrophobic mismatch with surrounding membrane matrix, we introduce the contact energy $U > 0$ between the nearest-neighbor raft patches. The total raft-raft contact energy then takes the form[54]

$$\mathrm{H}_{\text{r-r}} = -U \sum_{\langle i,j \rangle} w_i w_j \tag{3}$$

which sums over all pairs of nearest-neighbor patches. The value of contact energy U is set up to $U = 1.2U^*$, where $U = 2\ln\left(1+\sqrt{2}\right)k_{\mathrm{B}}T$, and the area fraction of lipid raft in cell membrane $x = \sum_i w_i / N = 0.1$ unless otherwise specified. In addition, the lipid rafts often exhibit larger bending rigidity than the surrounding membrane matrix, i.e., $\kappa_{\mathrm{r}} > \kappa_{\mathrm{m}}$ because of the difference in lipid composition (Effect of cholesterol on the rigidity of saturated and unsaturated membranes: fluctuation and electrodeformation analysis of giant vesicles). This bending rigidity contrast affects the membrane elastic energy according to Eq. (1). In our study, we take the bending rigidity $\kappa_{\mathrm{m}} = 25k_{\mathrm{B}}T$ for membrane matrix, and $\kappa_{\mathrm{r}} = 5.0\kappa_{\mathrm{m}}$ for raft patches taking into account the bending rigidity contrast[61,62].

The Hamiltonian $\mathrm{H} = \mathrm{H}_{\mathrm{el}} + \mathrm{H}_{\mathrm{in}} + \mathrm{H}_{\text{r-r}}$ defines the membrane-cytoskeleton system. We employ Monte Carlo (MC) method to study the system response to membrane tension and pressure. There are three types of trial moves involved in system configuration evolution: (i) vertical movement of membrane patches to capture the thermal shape fluctuations of cell membrane, (ii) lateral translations of proteins and

`

(iii) raft patches to mimic their diffusion. In each MC simulation, we attempt to shift every membrane patch to a new position, and then separately move proteins and raft patches to one of the four neighboring lattice sites. Trial moves of type (i) can lead to the change in the energy term H_{el} and H_{in}, type (ii) in H_{in}, and type (iii) in $H_{r\text{-}r}$. These trial moves are accepted or not according to the Metropolis algorithm. Especially, to prevent the membrane and cytoskeleton from overlapping, trial moves of type (i) leading to $l_i < 0$ will be rejected. The proportion of the three types of attempted motions in each MC step is chosen according to their physical time scales[62].

We perform simulation with membrane size up to $N = 100 \times 100$ patches. At the beginning of each simulation, both proteins and lipid rafts are randomly distributed in the cell membrane. The membrane-cytoskeleton system is allowed to relax to thermal equilibration with 5×10^7 MC steps, followed by a subsequent run of 5×10^7 MC steps for statistical sampling.

Quantification and statistical analysis

Statistical analyses for all experiments were performed in Prism (GraphPad) v5.02. Statistical data are presented as median or mean $\pm$ SEM, SD. Statistical tests used and p values are specified in the figure legends. Samples in most cases were defined as the number of cells counted/examined within multiple different fields of view on the same dish/slide, and thus represent data from a single sample within a single experiment that are representative of at least three additional independently conducted experiments.

`

ACKNOWLEDGEMENT

This study was supported by the National Natural Science Foundation of China (NSFC) (12222201, 82273500, 82372750, 12332019, U20A20390), the National Key R&D Program of China (2023YFC2507000), Fundamental Research Funds for the Central Universities (ZG140S1971, KG16228501) and the CAMS Innovation Fund for Medical Sciences (2023-I2M-3-003 and 2022-I2M-1-008).

AUTHOR CONTRIBUTIONS

J. D., Y.B.F., and Y.Z. designed and supervised the experiments. X.B.Z., M.T., and X.H.W. performed the experiments. L.L., X.H.W. and X.B.L developed the computational model. All the authors took part in the data analysis. X.B.Z. and J.D. wrote the paper.

CONFLICTS OF INTEREST

Authors declare that there are no conflicts to declare.

`

REFERENCES

1. Eisenhoffer, G.T., Loftus, P.D., Yoshigi, M., Otsuna, H., Chien, C.B., Morcos, P.A., and Rosenblatt, J. (2012). Crowding induces live cell extrusion to maintain homeostatic cell numbers in epithelia. Nature *484*, 546-549. 10.1038/nature10999.
2. Nia, H.T., Munn, L.L., and Jain, R.K. (2020). Physical traits of cancer. Science *370*. 10.1126/science.aaz0868.
3. Wirtz, D., Konstantopoulos, K., and Searson, P.C. (2011). The physics of cancer: the role of physical interactions and mechanical forces in metastasis. Nat Rev Cancer *11*, 512-522. 10.1038/nrc3080.
4. van Helvert, S., Storm, C., and Friedl, P. (2018). Mechanoreciprocity in cell migration. Nat Cell Biol *20*, 8-20. 10.1038/s41556-017-0012-0.
5. Tse, J.M., Cheng, G., Tyrrell, J.A., Wilcox-Adelman, S.A., Boucher, Y., Jain, R.K., and Munn, L.L. (2012). Mechanical compression drives cancer cells toward invasive phenotype. Proc Natl Acad Sci U S A *109*, 911-916. 10.1073/pnas.1118910109.
6. Jain, R.K., Martin, J.D., and Stylianopoulos, T. (2014). The role of mechanical forces in tumor growth and therapy. Annu Rev Biomed Eng *16*, 321-346. 10.1146/annurev-bioeng-071813-105259.
7. Bansaccal, N., Vieugue, P., Sarate, R., Song, Y., Minguijon, E., Miroshnikova, Y.A., Zeuschner, D., Collin, A., Allard, J., Engelman, D., et al. (2023). The extracellular matrix dictates regional competence for tumour initiation. Nature *623*, 828-835. 10.1038/s41586-023-06740-y.
8. Liu, Y.J., Le Berre, M., Lautenschlaeger, F., Maiuri, P., Callan-Jones, A., Heuze, M., Takaki, T., Voituriez, R., and Piel, M. (2015). Confinement and low adhesion induce fast amoeboid migration of slow mesenchymal cells. Cell *160*, 659-672. 10.1016/j.cell.2015.01.007.
9. Ruprecht, V., Wieser, S., Callan-Jones, A., Smutny, M., Morita, H., Sako, K., Barone, V., Ritsch-Marte, M., Sixt, M., Voituriez, R., and Heisenberg, C.P. (2015). Cortical contractility triggers a stochastic switch to fast amoeboid cell motility. Cell *160*, 673-685. 10.1016/j.cell.2015.01.008.
10. Lomakin, A.J., Cattin, C.J., Cuvelier, D., Alraies, Z., Molina, M., Nader, G.P.F., Srivastava, N., Saez, P.J., Garcia-Arcos, J.M., Zhitnyak, I.Y., et al. (2020). The nucleus acts as a ruler tailoring cell responses to spatial constraints. Science *370*. 10.1126/science.aba2894.
11. Venturini, V., Pezzano, F., Catala Castro, F., Hakkinen, H.M., Jimenez-Delgado, S., Colomer-Rosell, M., Marro, M., Tolosa-Ramon, Q., Paz-Lopez, S., Valverde, M.A., et al. (2020). The nucleus measures shape changes for cellular proprioception to control dynamic cell behavior. Science *370*. 10.1126/science.aba2644.
12. Nader, G.P.F., Aguera-Gonzalez, S., Routet, F., Gratia, M., Maurin, M., Cancila, V., Cadart, C., Palamidessi, A., Ramos, R.N., San Roman, M., et al. (2021). Compromised nuclear envelope integrity drives TREX1-dependent DNA damage and tumor cell invasion. Cell *184*, 5230-5246 e5222. 10.1016/j.cell.2021.08.035.
13. Cambria, E., Coughlin, M.F., Floryan, M.A., Offeddu, G.S., Shelton, S.E., and Kamm, R.D. (2024). Linking cell mechanical memory and cancer metastasis. Nature Reviews Cancer. 10.1038/s41568-023-00656-5.
14. Nasrollahi, S., Walter, C., Loza, A.J., Schimizzi, G.V., Longmore, G.D., and Pathak, A. (2017). Past matrix stiffness primes epithelial cells and regulates their future collective migration

`

through a mechanical memory. Biomaterials *146*, 146-155. 10.1016/j.biomaterials.2017.09.012.

15. Watson, A.W., Grant, A.D., Parker, S.S., Hill, S., Whalen, M.B., Chakrabarti, J., Harman, M.W., Roman, M.R., Forte, B.L., Gowan, C.C., et al. (2021). Breast tumor stiffness instructs bone metastasis via maintenance of mechanical conditioning. Cell Reports *35*. 10.1016/j.celrep.2021.109293.
16. Messal, H.A., Alt, S., Ferreira, R.M.M., Gribben, C., Wang, V.M., Cotoi, C.G., Salbreux, G., and Behrens, A. (2019). Tissue curvature and apicobasal mechanical tension imbalance instruct cancer morphogenesis. Nature *566*, 126-130. 10.1038/s41586-019-0891-2.
17. Eckert, M.A., Lwin, T.M., Chang, A.T., Kim, J., Danis, E., Ohno-Machado, L., and Yang, J. (2011). Twist1-induced invadopodia formation promotes tumor metastasis. Cancer Cell *19*, 372-386. 10.1016/j.ccr.2011.01.036.
18. Murphy, D.A., and Courtneidge, S.A. (2011). The 'ins' and 'outs' of podosomes and invadopodia: characteristics, formation and function. Nat Rev Mol Cell Biol *12*, 413-426. 10.1038/nrm3141.
19. Eddy, R.J., Weidmann, M.D., Sharma, V.P., and Condeelis, J.S. (2017). Tumor Cell Invadopodia: Invasive Protrusions that Orchestrate Metastasis. Trends Cell Biol *27*, 595-607. 10.1016/j.tcb.2017.03.003.
20. Li, C.X., Talele, N.P., Boo, S., Koehler, A., Knee-Walden, E., Balestrini, J.L., Speight, P., Kapus, A., and Hinz, B. (2017). MicroRNA-21 preserves the fibrotic mechanical memory of mesenchymal stem cells. Nature Materials *16*, 379-389. 10.1038/nmat4780.
21. Yang, C., Tibbitt, M.W., Basta, L., and Anseth, K.S. (2014). Mechanical memory and dosing influence stem cell fate. Nature Materials *13*, 645-652. 10.1038/nmat3889.
22. Stemmler, M.P., Eccles, R.L., Brabletz, S., and Brabletz, T. (2019). Non-redundant functions of EMT transcription factors. Nat Cell Biol *21*, 102-112. 10.1038/s41556-018-0196-y.
23. Lipowsky, R. (2021). Remodeling of Membrane Shape and Topology by Curvature Elasticity and Membrane Tension. Advanced Biology *6*. 10.1002/adbi.202101020.
24. Colom, A., Derivery, E., Soleimanpour, S., Tomba, C., Molin, M.D., Sakai, N., Gonzalez-Gaitan, M., Matile, S., and Roux, A. (2018). A fluorescent membrane tension probe. Nat Chem *10*, 1118-1125. 10.1038/s41557-018-0127-3.
25. Bisaria, A., Hayer, A., Garbett, D., Cohen, D., and Meyer, T. (2020). Membrane-proximal F-actin restricts local membrane protrusions and directs cell migration. Science *368*, 1205-1210. 10.1126/science.aay7794.
26. Fritz, R.D., Menshykau, D., Martin, K., Reimann, A., Pontelli, V., and Pertz, O. (2015). SrGAP2-Dependent Integration of Membrane Geometry and Slit-Robo-Repulsive Cues Regulates Fibroblast Contact Inhibition of Locomotion. Dev Cell *35*, 78-92. 10.1016/j.devcel.2015.09.002.
27. Fritz, R.D., Letzelter, M., Reimann, A., Martin, K., Fusco, L., Ritsma, L., Ponsioen, B., Fluri, E., Schulte-Merker, S., van Rheenen, J., and Pertz, O. (2013). A Versatile Toolkit to Produce Sensitive FRET Biosensors to Visualize Signaling in Time and Space. *6*, rs12-rs12. doi:10.1126/scisignal.2004135.
28. Liu, B., Chrzanowska, M., and Burridge, K. (2019). Regulation of Cell Contractility by RhoA: Stress Fiber and Focal Adhesion Assembly. In pp. 245-262. 10.1201/9780429129384-17.
29. Sathe, M., Muthukrishnan, G., Rae, J., Disanza, A., Thattai, M.A.-O., Scita, G.A.-O., Parton,

`

R.A.-O., and Mayor, S. Small GTPases and BAR domain proteins regulate branched actin polymerisation for clathrin and dynamin-independent endocytosis.

30. Wang, X., Li, L., Shao, Y., Wei, J., Song, R., Zheng, S., Li, Y., and Song, F. (2021). Effects of the Laplace pressure on the cells during cytokinesis. iScience *24*, 102945. 10.1016/j.isci.2021.102945.
31. Petrie, R.J., and Koo, H. (2014). Direct Measurement of Laplace Pressure. Current Protocols in Cell Biology *63*. 10.1002/0471143030.cb1209s63.
32. Tsujita, K., Satow, R., Asada, S., Nakamura, Y., Arnes, L., Sako, K., Fujita, Y., Fukami, K., and Itoh, T. (2021). Homeostatic membrane tension constrains cancer cell dissemination by counteracting BAR protein assembly. Nat Commun *12*, 5930. 10.1038/s41467-021-26156-4.
33. Lingwood, D., and Simons, K. (2010). Lipid rafts as a membrane-organizing principle. Science *327*, 46-50. 10.1126/science.1174621.
34. Sezgin, E., Levental, I., Mayor, S., and Eggeling, C. (2017). The mystery of membrane organization: composition, regulation and roles of lipid rafts. Nat Rev Mol Cell Biol *18*, 361-374. 10.1038/nrm.2017.16.
35. Martinez-Outschoorn, U.E., Sotgia, F., and Lisanti, M.P. (2015). Caveolae and signalling in cancer. Nat Rev Cancer *15*, 225-237. 10.1038/nrc3915.
36. Kabbani, A.M., Raghunathan, K., Lencer, W.I., Kenworthy, A.K., and Kelly, C.V. (2020). Structured clustering of the glycosphingolipid GM1 is required for membrane curvature induced by cholera toxin. Proceedings of the National Academy of Sciences *117*, 14978-14986. 10.1073/pnas.2001119117.
37. Yoon, T.Y., Jeong, C., Lee, S.W., Kim, J.H., Choi, M.C., Kim, S.J., Kim, M.W., and Lee, S.D. (2006). Topographic control of lipid-raft reconstitution in model membranes. Nat Mater *5*, 281-285. 10.1038/nmat1618.
38. Dongre, A., and Weinberg, R.A. (2019). New insights into the mechanisms of epithelial–mesenchymal transition and implications for cancer. Nature Reviews Molecular Cell Biology *20*, 69-84. 10.1038/s41580-018-0080-4.
39. Proceedings of the National Academy of Sciences. 10.1073/pnas.
40. Otani, T., and Furuse, M. (2020). Tight Junction Structure and Function Revisited. Trends in Cell Biology *30*, 805-817. 10.1016/j.tcb.2020.08.004.
41. Marinari, E., Mehonic, A., Curran, S., Gale, J., Duke, T., and Baum, B. (2012). Live-cell delamination counterbalances epithelial growth to limit tissue overcrowding. Nature *484*, 542-545. 10.1038/nature10984.
42. Eisenhoffer, G.T., and Rosenblatt, J. (2013). Bringing balance by force: live cell extrusion controls epithelial cell numbers. Trends in Cell Biology *23*, 185-192. 10.1016/j.tcb.2012.11.006.
43. Dr. R. Jahir Hussain, V.S.D., P. Rengarajan (2012). Analysing the invasiveness of skin cancer using fractals. International Journal of Engineering Research and Applications *2*, 2068-2075.
44. Guz, N.V., Dokukin, M.E., Woodworth, C.D., Cardin, A., and Sokolov, I. (2015). Towards early detection of cervical cancer: Fractal dimension of AFM images of human cervical epithelial cells at different stages of progression to cancer. Nanomedicine *11*, 1667-1675. 10.1016/j.nano.2015.04.012.
45. Levental, I., Levental, K.R., and Heberle, F.A. (2020). Lipid Rafts: Controversies Resolved, Mysteries Remain. Trends Cell Biol *30*, 341-353. 10.1016/j.tcb.2020.01.009.

`

46. Viola, A., and Gupta, N. (2007). Tether and trap: regulation of membrane-raft dynamics by actin-binding proteins. Nat Rev Immunol *7*, 889-896. 10.1038/nri2193.
47. Yamaguchi, H., Takeo, Y., Yoshida, S., Kouchi, Z., Nakamura, Y., and Fukami, K. (2009). Lipid rafts and caveolin-1 are required for invadopodia formation and extracellular matrix degradation by human breast cancer cells. Cancer Res *69*, 8594-8602. 10.1158/0008-5472.CAN-09-2305.
48. Donatello, S., Babina, I.S., Hazelwood, L.D., Hill, A.D., Nabi, I.R., and Hopkins, A.M. (2012). Lipid raft association restricts CD44-ezrin interaction and promotion of breast cancer cell migration. Am J Pathol *181*, 2172-2187. 10.1016/j.ajpath.2012.08.025.
49. Simanshu, D.K., Philips, M.R., and Hancock, J.F. (2023). Consensus on the RAS dimerization hypothesis: Strong evidence for lipid-mediated clustering but not for G-domain-mediated interactions. Mol Cell *83*, 1210-1215. 10.1016/j.molcel.2023.03.008.
50. Zhou, Y., and Hancock, J.F. (2023). RAS nanoclusters are cell surface transducers that convert extracellular stimuli to Laplace signalling. FEBS Lett *597*, 892-908. 10.1002/1873-3468.14569.
51. Qi, Y., Ingólfsson, H.I., Cheng, X., Lee, J., Marrink, S.J., and Im, W. (2015). CHARMM-GUI Martini Maker for Coarse-Grained Simulations with the Martini Force Field. Journal of Chemical Theory and Computation *11*, 4486-4494. 10.1021/acs.jctc.5b00513.
52. Marrink, S.J., Risselada, H.J., Yefimov, S., Tieleman, D.P., and de Vries, A.H. (2007). The MARTINI Force Field: Coarse Grained Model for Biomolecular Simulations. The Journal of Physical Chemistry B *111*, 7812-7824. 10.1021/jp071097f.
53. Abraham, M.J., Murtola, T., Schulz, R., Páll, S., Smith, J.C., Hess, B., and Lindahl, E. (2015). GROMACS: High performance molecular simulations through multi-level parallelism from laptops to supercomputers. SoftwareX *1-2*, 19-25. 10.1016/j.softx.2015.06.001.
54. Risselada, H.J., and Marrink, S.J. (2008). The molecular face of lipid rafts in model membranes. Proceedings of the National Academy of Sciences *105*, 17367-17372. 10.1073/pnas.0807527105.
55. Humphrey, W., Dalke, A., and Schulten, K. (1996). VMD: Visual molecular dynamics. Journal of Molecular Graphics *14*, 33-38. https://doi.org/10.1016/0263-7855(96)00018-5.
56. Hassan, R., Garzon, M.A., Gao, W., and Ahmadpoor, F. (2024). Entropic pressure on fluctuating solid membranes. Journal of the Mechanics and Physics of Solids *183*, 105523. https://doi.org/10.1016/j.jmps.2023.105523.
57. Costa, M.N., Radhakrishnan, K., and Edwards, J.S. (2011). Monte Carlo simulations of plasma membrane corral-induced EGFR clustering. Journal of Biotechnology *151*, 261-270. 10.1016/j.jbiotec.2010.12.009.
58. Xu, G., Liu, Z., and Gao, H. (2016). Tension-compression asymmetry in the binding affinity of membrane-anchored receptors and ligands. Physical Review E *93*. 10.1103/PhysRevE.93.032411.
59. Li, L., Hou, R., Shi, X., Ji, J., Różycki, B., Hu, J., and Song, F. (2024). Control of cell membrane receptor condensation by adhesion to supported bilayers with nanoscale topography. Communications Physics *7*, 174. 10.1038/s42005-024-01670-1.
60. Li, L., Hu, J., Różycki, B., and Song, F. (2020). Intercellular Receptor–Ligand Binding and Thermal Fluctuations Facilitate Receptor Aggregation in Adhering Membranes. Nano Letters *20*, 722-728. 10.1021/acs.nanolett.9b04596.
61. Li, L., Hu, J., Shi, X., Różycki, B., and Song, F. (2021). Interplay between cooperativity of

`

intercellular receptor–ligand binding and coalescence of nanoscale lipid clusters in adhering membranes. Soft Matter *17*, 1912-1920. 10.1039/d0sm01904f.

62. Gracià, R.S., Bezlyepkina, N., Knorr, R.L., Lipowsky, R., and Dimova, R. (2010). Effect of cholesterol on the rigidity of saturated and unsaturated membranes: fluctuation and electrodeformation analysis of giant vesicles. Soft Matter *6*. 10.1039/b920629a.

`

Suppl Figures

Figure 1

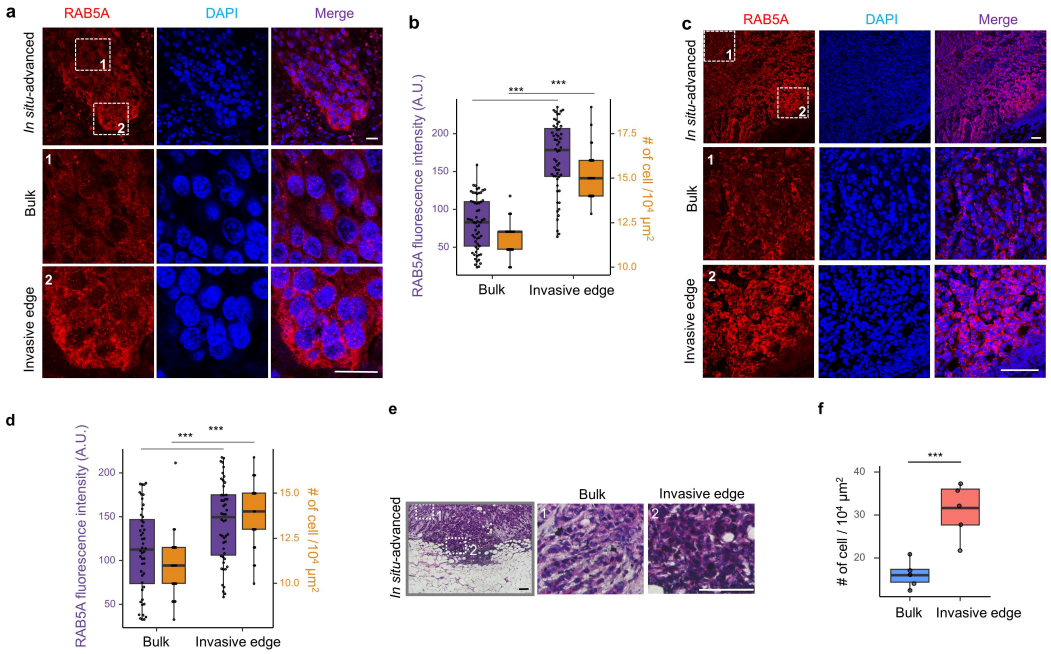

Figure 1. Overcrowding conditions of tumor cells in bulk and invasive edge. (**a**) Immunofluorescence of in human cervical cancer tissues. RAB5A (red), DAPI (blue). Scale bar: 20 μm. (**b**) Boxplot of nuclei number in per unit area (10e4 μm^2) and RAB5A fluorescence intensity from bulk and invasive edge focus. (**c**) Immunofluorescence of in situ advanced human primary breast tumors. RAB5A (red), DAPI (blue). Scale bar: 100 μm. (**d**) Boxplot of nuclei number in per unit area (10e4 μm^2) and RAB5A fluorescence intensity from bulk and invasive edge focus. **(e)** Hematoxylin&eosin stained in situ advanced human primary breast tumors. Scale bar: 100 μm. **(f)** Boxplot of nuclei number in per unit area (10e4 μm^2) from bulk and invasive edge focus. Data are presented as scatter plot of 5 individual tumor samples. ***$p < 0.005$; two-tailed unpaired t test.

`

Figure 2

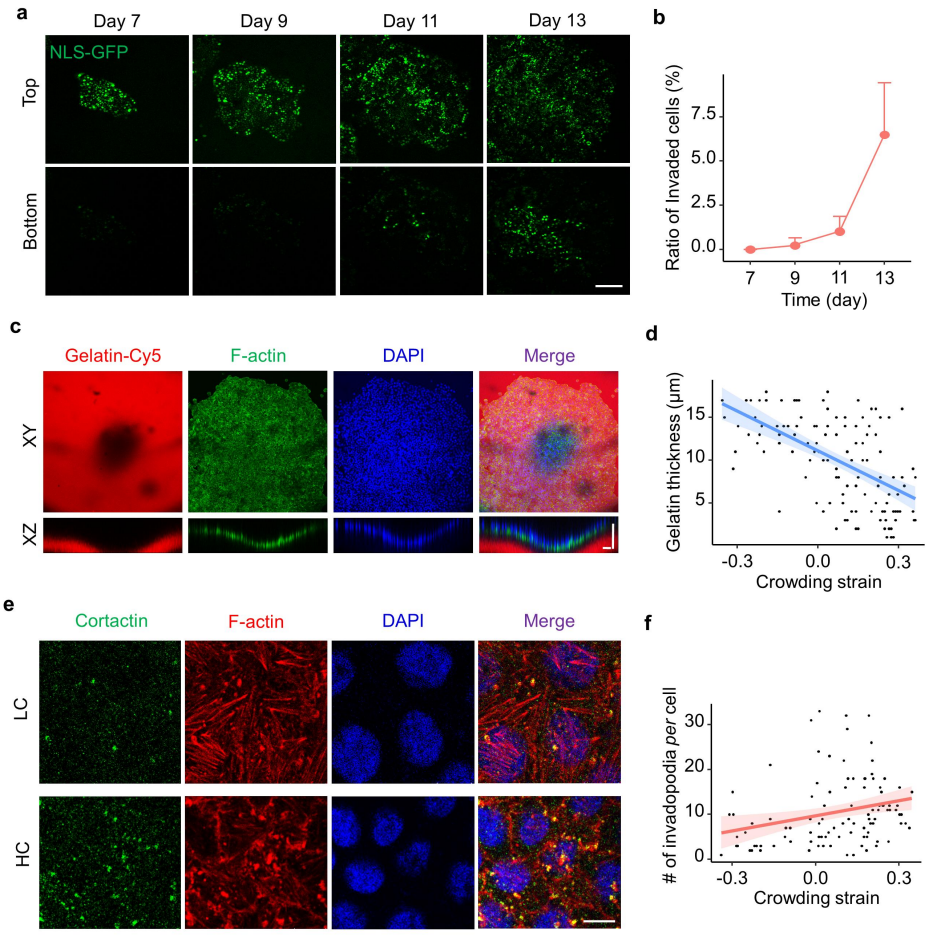

Figure 2. Overcrowding drives tumor cell invasion in a time-dependent way. (**a**) Representative XY slice images of Transwell Matrigel invasion assay in a growing monoclonal NLS-GFP positive HeLa cell sheet captured at the indicated time after seeding. Scale bar: 200 μm. (**b**) The ratio of invaded cells in NLS-GFP positive HeLa sheets was analyzed (means ± SD). (**c**) HeLa cells were plated on Cy5-conjugated gelatin hydrogels (red) for a growing monoclonal HeLa cell sheet. F-actin was stained with phalloidin and nuclei with DAPI. Scale bar: 50 μm. (**d**) Quantification of correlation between Cy5-conjugated gelatin thickness located in per cell and its crowding strain. (**e**) Representative XY slice image of cortactin (an invadopodium marker) and F-actin stained by cortactin and phalloidin, in LC and HC regions of HeLa cell sheet. Scale bar: 10 μm. (**f**) Quantification of invadopodia density per cell with corresponding crowding strain in panel (e).

`

Figure 3

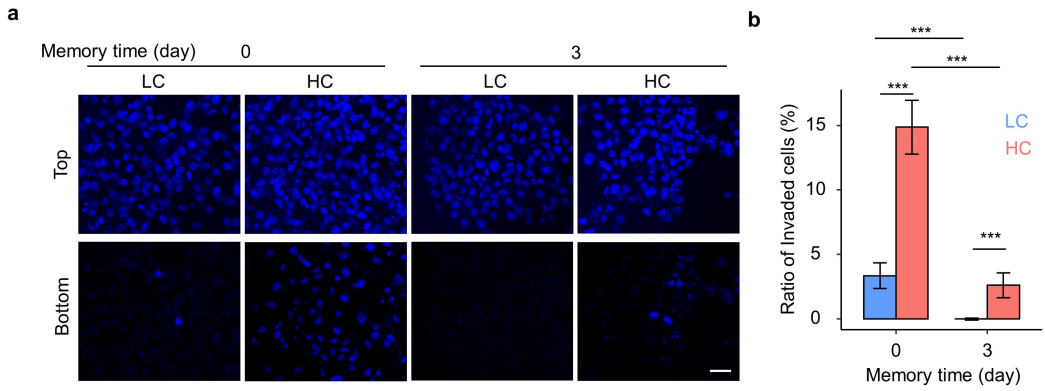

Figure 3. Overcrowding induces retentive invasiveness in A431 cells. (**a**) Transwell matrigel invasion assay of A431 cells after LC/HC culture for 5 days and sparse culture for 0 and 3 days. Representative DAPI images of cells that accumulated on the top and bottom surface. Scale bar: 50 µm. (**b**) The ratio of invaded cells in LC and HC of A431 cells in panel (a). Data are presented as ***$p < 0.005$; two-tailed unpaired t test.

`

Figure 4

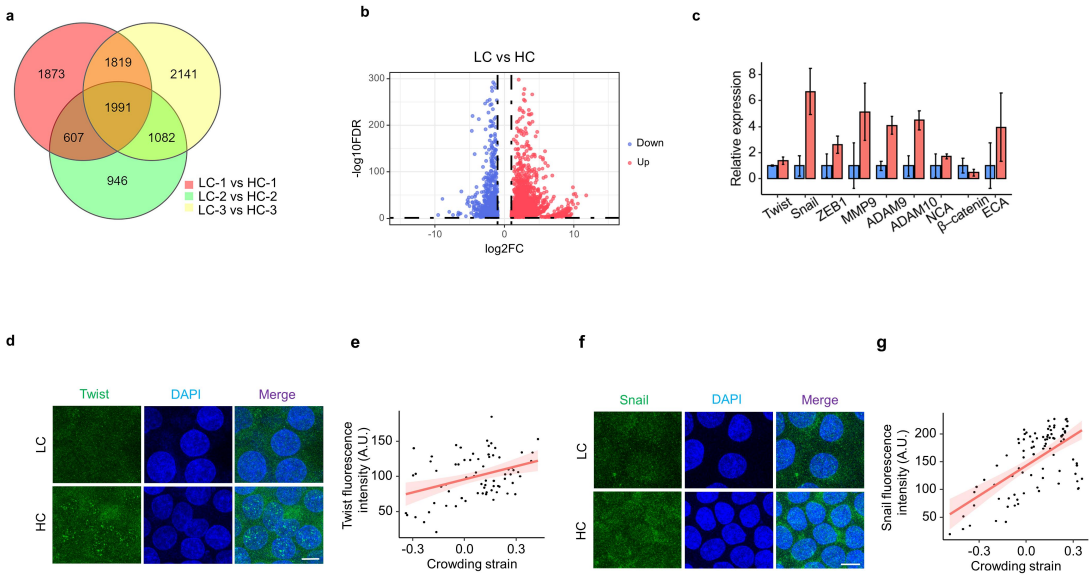

Figure 4. Overcrowding affects related EMT gene expression in cancer cells. (a) Venn diagram of different expression of genes between different comparison groups. The Venn diagrams show the number of unique genes and the number of commonly shared genes found in LC and HC groups. (**b**) Volcano plot shows genes differentially expressed between LC and HC. Each dot represents a gene; genes in red are up, genes in blue are down-regulated. **(c)** Boxplots showing mRNA expression data for Twist, Snail2, ZEB1, MMP9, ADAM9, ADAM10 and β-catenin in LC and HC HeLa cells as determined by SMART seq II data respectively. (**d**) Representative XY slice image of Twist, F-actin and nucleus stained by Twist, phalloidin and DAPI, respectively, in the low and high crowding regions of HeLa cell sheet. Scale bar: 10 μm. (**e**) Quantification of Twist fluorescence intensity in per cell based on crowding strain. (**f**) Representative XY slice image of Snail, F-actin and nucleus stained by snail, phalloidin and DAPI, respectively, in the low and high crowding regions of HeLa cell sheet. Scale bar: 10 μm. (**g**) Quantification of Snail fluorescence intensity in per cell based on crowding strain.

`

Figure 5

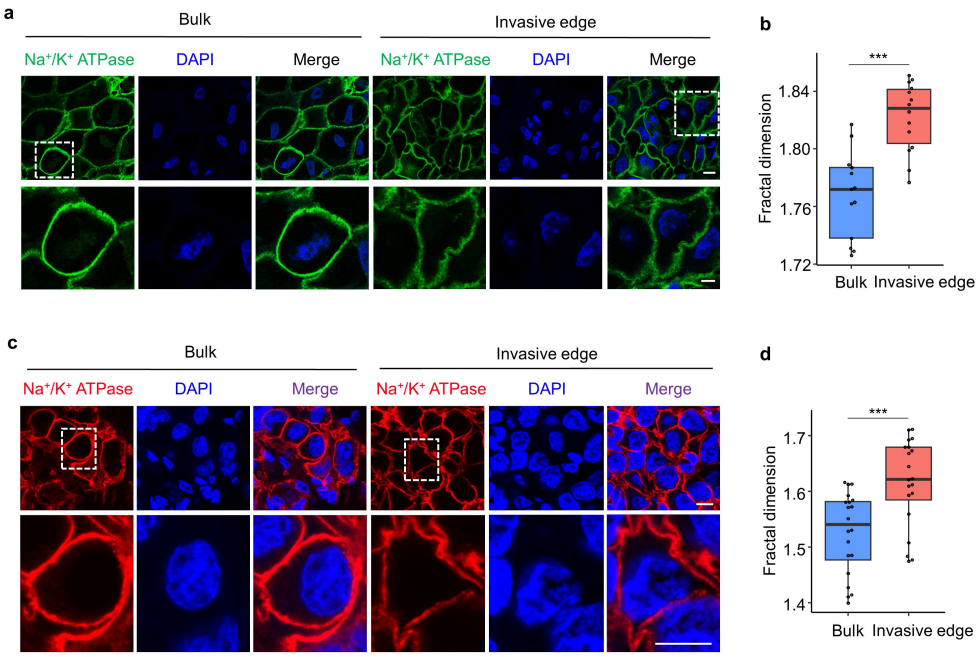

Figure 5. Overcrowding triggers nanocorrugated topographical transition of plasma membrane in human cancer tissues. (**a**) Representative XY slice image of sodium potassium ATPase (green) and nucleus (blue) in the low and high crowded regions of cervical cancer tissues. Scale bar: 10 μm. (**b**) Quantitation of correlation between fractal dimension in per cell of human cervical cancer tissue and its crowding strain. (**c**) Representative XY slice image of sodium potassium ATPase (red) and nucleus (blue) in the low and high crowded regions of breast tumors. Scale bar: 10 μm. (**d**) Quantitation of correlation between fractal dimension in per cell of human breast cancer tissue and its crowding strain. Data are presented as ***$p < 0.005$; two-tailed unpaired t test.

`

Figure 6

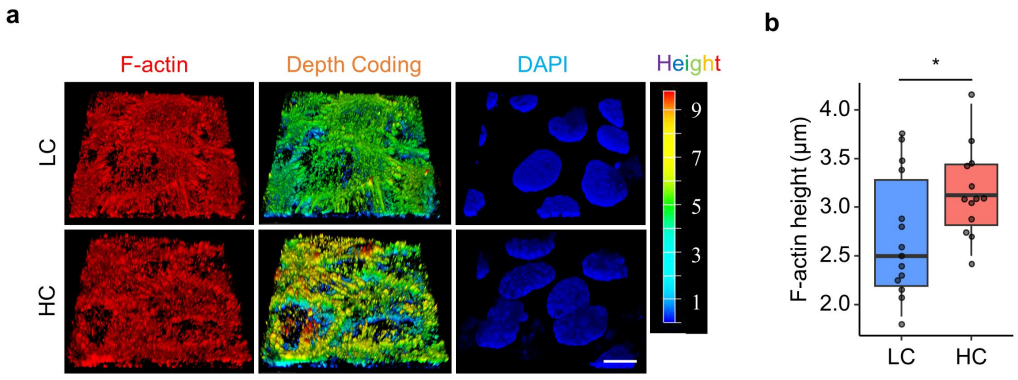

Figure 6. Overcrowding triggers F-actin remodeling at the apical membrane in A431 cells. (**a**) Confocal 3D reconstruction of the apical membrane of LC and HC A431 cells fixed and stained for F-actin. Scale bar: 10 µm. (**b**) Quantification of the average height of F-actin from the apical membrane in LC and HC A431 cells. Data are presented as *$p < 0.05$; two-tailed unpaired t test.

`

Figure 7

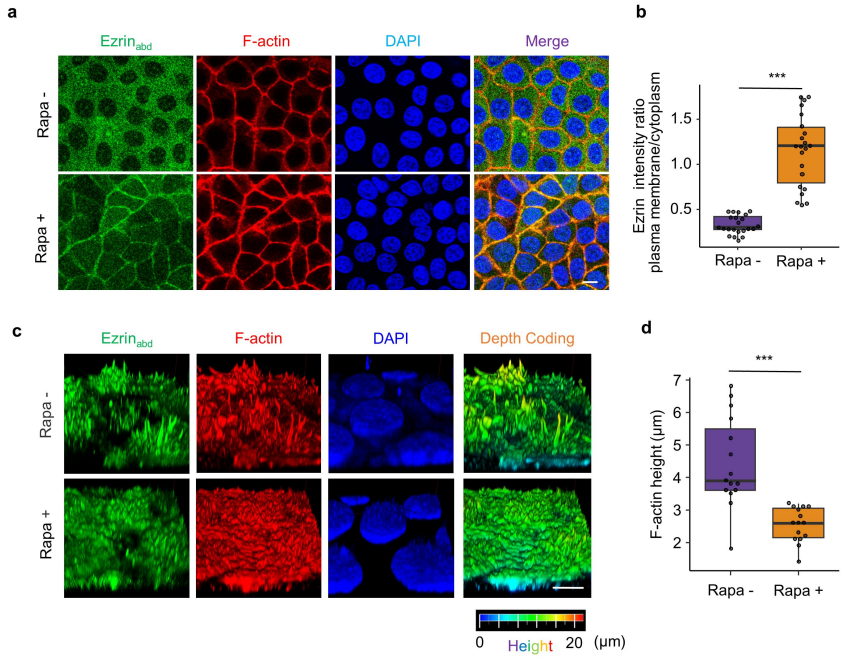

Figure 7. Suppressing F-actin remodeling at the apical membrane by enhancing ERM-mediated MCA. (**a**) Immunofluorescence analysis of EzrinabdT567D location (green) in FKBP-EzrinabdT567D^{+} HeLa cells treated with rapamycin or vehicle. Scale bar: 10 µm. (**b**) Quantification of EzrinabdT567D intensity plasma membrane/cytoplasm ratio in FKBP-EzrinabdT567D^{+} cells. (**c**) Confocal 3D reconstruction of the apical membrane of FKBP-EzrinabdT567D^{+} HeLa cells treated with rapamycin or vehicle. Scale bar: 10 µm. (**d**) Quantification of the average height of F-actin from the apical membrane in FKBP-EzrinabdT567D^{+} HeLa cells treated with rapamycin or vehicle. Data are presented as ***$p < 0.005$; two-tailed unpaired t test.

`

Figure 8

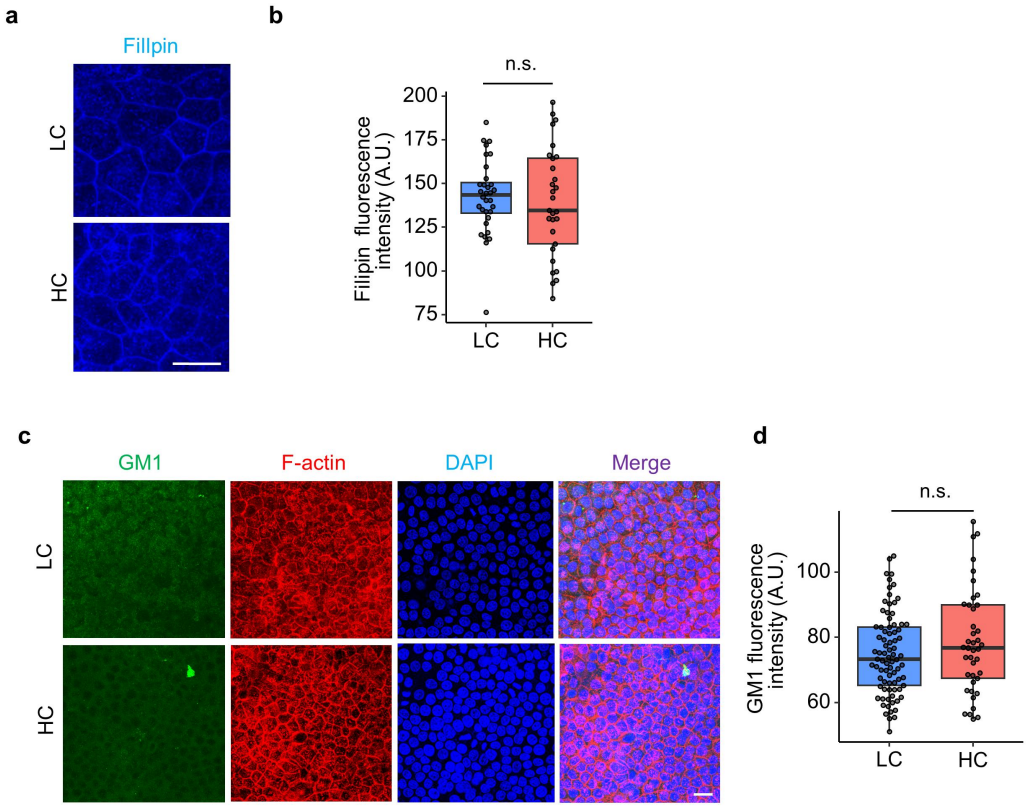

Figure 8. Overcrowding does not affect the levels of main components within lipid rafts in cancer cells. (a) Representative XY confocal images showing filipin staining of cholesterol in different crowding regions of monoclonal HeLa cell sheet. Scale bar: 20 µm. **(b)** Quantitation of filipin fluorescence intensity in low and high crowding HeLa cells. **(c)** Representative XY confocal images showing immunostaining for GM1 in different crowding regions of monoclonal HeLa cell sheet. Scale bar: 20 µm. **(d)** Quantitation of GM1 fluorescence intensity in LC and HC HeLa cells . Data are presented as mean ± SEM. Data are presented as n.s., not significant; two-tailed unpaired t test.

`